Draft version July 21, 2025
Typeset using LaTeX **twocolumn** style in AASTeX7.0.1

arXiv:2507.13409v1 [astro-ph.EP] 17 Jul 2025

NSF-DOE Vera C. Rubin Observatory Observations of Interstellar Comet 3I/ATLAS (C/2025 N1)

Colin Orion Chandler [1,2,3] Pedro H. Bernardinelli [2,*] Mario Jurić [2] Devanshi Singh [2]
Henry H. Hsieh [4] Ian Sullivan [2] R. Lynne Jones [5,6] Jacob A. Kurlander [2] Dmitrii Vavilov [2]
Siegfried Eggl [7,8] Matthew Holman [9] Federica Spoto [10] Megan E. Schwamb [11]
Eric J. Christensen [5] Wilson Beebe [1,2] Aaron Roodman [12] Kian-Tat Lim [12] Tim Jenness [13]
James Bosch [14] Brianna Smart [2] Eric Bellm [2] Sean MacBride [15] Meredith L. Rawls [2,5]
Sarah Greenstreet [16,2] Colin Slater [2] Aren Heinze [2] Željko Ivezić [2] Bob Blum [16]
Andrew Connolly [2] Gregory Daues [17] Rahil Makadia [7] Michelle Gower [18,8] J. Bryce Kalmbach [12]
David Monet [19] Michele T. Bannister [20] Luke Dones [21] Rosemary C. Dorsey [22]
Wesley C. Fraser [23,24] John C. Forbes [20] Cesar Fuentes [25] Carrie E. Holt [26,†] Laura Inno [27,28]
Geraint H. Jones [29] Matthew M. Knight [30] Chris J. Lintott [31] Tim Lister [26] Robert Lupton [14]
Mark Jesus Mendoza Magbanua [32] Renu Malhotra [33] Beatrice E. A. Mueller [4] Joseph Murtagh [11]
Nitya Pandey [25] William T. Reach [34] Nalin H. Samarasinha [4] Darryl Z. Seligman [35,‡]
Colin Snodgrass [36] Michael Solontoi [37] Gyula M. Szabó [38,39] Ellie White [40] Maria Womack [41]
Leslie A. Young [21] Russ Allbery [13] Roberto Armellin [42] Éric Aubourg [43] Chrysa Avdellidou [44]
Farrukh Azfar,[31] James Bauer [45] Keith Bechtol [13,46] Matthew Belyakov [47] Susan D. Benecchi [4]
Ivano Bertini [48] Bryce T. Bolin [49] Maitrayee Bose [50] Laura E. Buchanan [24] Alexandre Boucaud [51]
Rodrigo C. Boufleur [52] Dominique Boutigny [53] Felipe Braga-Ribas [54,52] Daniel Calabrese,[55]
J. I. B. Camargo [56,52] Neven Caplar [2] Benoit Carry [57] Juan Pablo Carvajal [58] Yumi Choi [16]
Luiz da Costa,[52] Preeti Cowan [59] Steve Croft [60,61,62] Matija Ćuk [62] Felipe Daruich [5]
Guillaume Daubard,[63] James R. A. Davenport [2] Tansu Daylan [64] Jennifer Delgado [65]
Hadrien A. R. Devillepoix [66,67] Peter E. Doherty [9] Abbie Donaldson [36] Holger Drass [5]
Stephanie JH Deppe [16,5] Gregory P. Dubois-Felsmann [68] Frossie Economou [13] Marielle R. Eduardo [24]
Ioana Sotuela Elorriaga,[5] Maxwell K. Frissell [2,3] Grigori Fedorets [69,22] Maryann Benny Fernandes [70]
Marco Fulle [71] David W. Gerdes [72] Alex R. Gibbs [33] A. Fraser Gillan [73] Leanne P. Guy [5]
Mark Hammergren [74] Andrew Hanushevsky [12] Fabio Hernandez [75] Daniel Hestroffer [76]
Matthew J. Hopkins [31,20] Mikael Granvik [22,77] Simone Ieva [78] David H. Irving [5,16] Buell T. Jannuzi [79]
M. James Jee,[80,81] David Jimenez [13] Altair Ramos Gomes-Júnior [82,52] Claire Juramy [83]
Steven M. Kahn [84] Arun Kannawadi [85] Yijung Kang [12,86] Agnieszka Kryszczyńska [87] Ivan Kotov [88]
Alec Koumjian [89] K.Simon Krughoff [13,§] Craig Lage [81] Travis J. Lange,[12] W. Garrett Levine [90]
Zhuofu Li [2] Shuang Liang,[12] Javier Licandro [91] Hsing Wen Lin (林省文) [92,93] Nate B. Lust [14]
Ryan R. Lyttle [11] Ashish A. Mahabal [94,95] Max Mahlke [96] Andrés A. Plazas Malagón [12,86]
Luis E. Salazar Manzano [97] Moniez Marc [98] Giuliano Margoti [56,52] Dušan Marčeta [99]
Mario D. Melita,[100] Felipe Menanteau [18] Joshua Meyers [86,12] Dave Millsc [13] Naomi Morato [2]
Surhud More [101] Christopher B. Morrison [102] Youssef Moulane [103] Marco A. Muñoz-Gutiérrez [104]
Newcomer F. M. [105] Paul O'Connor [88] Drew Oldag [1,2] William J Oldroyd [3] William O'Mullane [5]
Cyrielle Opitom [36] Dagmara Oszkiewicz [87] Gary L. Page [106] Jack Patterson [20] Matthew J. Payne [9]
Julien Peloton [98] Chrystian Luciano Pereira [56,52] John R. Peterson [107] Daniel Polin [81]
Hannah Mary Margaret Pollek,[12] Rebekah Polen,[85] Yongqiang Qiu,[12] Darin Ragozzine [108]
Jayadev Rajagopal [16] Wouter van Reeven,[55] Malena Rice [109] Stephen T. Ridgway [16]
Andrew S. Rivkin [110] James E. Robinson [36] Agata Rożek [36] Andrei Salnikov [12] Bruno O. Sánchez [111]
Gal Sarid [112] Charles A. Schambeau [113,41] German Schumacher,[5,16] Daniel Scolnic [85,70]
Rafe H. Schindler,[86,12] Robert Seaman [33] Šebag Jacques [55] Richard A. Shaw [114] Alysha Shugart [5,16]
Jonathan Sick [115,13] Amir Siraj [14] Michael C. Sitarz [116] Shahram Sobhani,[55] Christine Soldahl,[12]
Brian Stalder [13] Steven Stetzler [2] John D. Swinbank [117] László Szigeti [118] Michael Tauraso [2]
Adam Thornton [55] Luca Tonietti [27,28] David E. Trilling [3] Chadwick A. Trujillo [3] Te-Wei Tsai [13]
Tony Tyson [81] Elana K. Urbach [119] Peter Vereš [9] Stelios Voutsinas [13] Charlotte Ward [14]

Corresponding author: Colin Orion Chandler
coc123@uw.edu

Maxine West [1,2] Ian Wong [114] W. M. Wood-Vasey [120] Bin Yang [121] Quanhzi Ye [45,122] and Jinshuo Zhang [2]

[1] LSST Interdisciplinary Network for Collaboration and Computing, Tucson, USA
[2] Dept. of Astronomy & the DiRAC Institute, University of Washington, Seattle, USA
[3] Department of Astronomy and Planetary Science, Northern Arizona University, Flagstaff, USA
[4] Planetary Science Institute, 1700 East Fort Lowell Rd., Suite 106, Tucson, AZ 85719, USA
[5] Vera C. Rubin Observatory, Avenida Juan Cisternas 1500, La Serena, Chile
[6] Aerotek, Victoria BC, Canada
[7] The Grainger College of Engineering, Department of Aerospace Engineering, University of Illinois Urbana-Champaign, Urbana, USA
[8] Department of Astronomy, University of Illinois at Urbana-Champaign, Urbana, IL 61801, USA
[9] Harvard-Smithsonian Center for Astrophysics, 60 Garden St., MS 51, Cambridge, MA 02138, USA
[10] Minor Planet Center – Center for Astrophysics, Harvard & Smithsonian, 60 Garden St., MS 15, Cambridge (MA), USA
[11] Astrophysics Research Centre, School of Mathematics and Physics, Queen's University Belfast, BT7 1NN, UK
[12] SLAC National Accelerator Laboratory, 2575 Sand Hill Rd., Menlo Park, CA 94025, USA
[13] Rubin Observatory Project Office, 950 N Cherry Ave, Tucson, AZ 85719
[14] Department of Astrophysical Sciences, Princeton University, Princeton, NJ 08544, USA
[15] Physik-Institut, University of Zurich, Winterthurerstrasse 190, 8057 Zurich, Switzerland
[16] NSF National Optical-Infrared Astronomy Research Laboratory, 950 North Cherry Avenue, Tucson, AZ 85719, USA
[17] Illinois Center for Advanced Studies of the Universe & Department of Physics, University of Illinois at Urbana-Champaign, Urbana, IL 61801, USA
[18] National Center for Supercomputing Applications, Urbana, IL, USA
[19] The United States Naval Observatory, 3450 Massachusetts Avenue, NW, Washington, DC 20392-5420.
[20] School of Physical and Chemical Sciences — Te Kura Matū, University of Canterbury, Private Bag 4800, Christchurch 8140, New Zealand
[21] Southwest Research Institute, 1301 Walnut Street, Suite 400, Boulder, DC 80302
[22] Department of Physics, P.O. Box 64, 00014 University of Helsinki, Finland
[23] National Research Council of Canada, Herzberg Astronomy and Astrophysics Research Centre, 5071 West Saanich Road, Victoria, BC V8T 1E7, Canada
[24] Department of Physics and Astronomy, University of Victoria, Elliott Building, 3800 Finnerty Road, Victoria, BC V8P 5C2, Canada
[25] Departamento de Astronomía, Universidad de Chile, Camino del Observatorio 1515, Las Condes, Santiago, Chile
[26] Las Cumbres Observatory, 6740 Cortona Drive Suite 102, Goleta, CA 93117, USA
[27] Department of Science and Technology, Parthenope University of Naples, Centro Direzionale C4 Island, 80143, Naples, Italy
[28] INAF, Osservatorio Astronomico di Capodimonte, Salita Moiariello, 16, Naples, I-80131, Italy.
[29] European Space Technology Centre (ESTEC), European Space Agency, Keplerlaan 1, 2200 AG Noordwijk, Netherlands; and Mullard Space Science Laboratory, University College London, Holmbury St. Mary, Dorking RH5 6NT, UK
[30] Physics Department, United States Naval Academy, Annapolis, MD 21402, USA
[31] Department of Physics, University of Oxford, Denys Wilkinson Building, Keble Road, Oxford, OX1 3RH, UK
[32] Dept. of Laboratory Medicine, University of California San Francisco, 2340 Sutter Street, San Francisco, CA 94143, USA
[33] Lunar and Planetary Laboratory, University of Arizona, 1629 E University Blvd, Tucson, AZ 85721
[34] Space Science Institute, 4765 Walnut St, Suite B, Boulder, CO 80301, USA
[35] Dept. of Physics and Astronomy, Michigan State University, East Lansing, MI 48824, USA
[36] Institute for Astronomy, University of Edinburgh Royal Observatory Edinburgh, Blackford Hill, Edinburgh, EH9 3HJ, UK
[37] Monmouth College, 700 E Broadway, Monmouth, IL 61462
[38] ELTE Eötvös Loránd University, Gothard Astrophysical Observatory, Szent Imre h. u. 112, 9700, Szombathely, Hungary
[39] Konkoly Observatory, HUN-REN Research Centre for Astronomy and Earth Sciences, Konkoly Thege 15-17, H-1121 Budapest, Hungary
[40] Marshall University, 1 John Marshall Drive, Huntington, WV 25755
[41] Department of Physics, University of Central Florida, 4111 Libra Drive, Physical Sciences Bldg. 430, Orlando, FL 32816-2385, USA
[42] The University of Auckland, 20 Symond Street, 1010 Auckland, New Zealand
[43] Université Paris Cité, CNRS, CEA, Astroparticule et Cosmologie, F-75013 Paris, France
[44] University of Leicester, School of Physics and Astronomy, University Road, LE1 7RH, Leicester, UK
[45] Department of Astronomy, University of Maryland College Park, MD 20742, USA
[46] Department of Physics, University of Wisconsin, Madison, 1150 University Avenue, Madison, WI 53706, USA
[47] Division of Geological and Planetary Sciences, California Institute of Technology, Pasadena, CA 91125, USA
[48] University Parthenope of Naples, Centro Direzionale Site, isola C4 Naples 80143, Italy
[49] Eureka Scientific, Oakland, CA 94602, U.S.A.
[50] School of Earth and Space Exploration, Arizona State University, Tempe AZ 85287
[51] Université Paris Cité, CNRS, Astroparticule et Cosmologie, F-75013 Paris, France

[52] *Laboratório Interinstitucional de e-Astronomia - LIneA, Av. Pastor Martin Luther King Jr, 126 Del Castilho, Nova América Offices, Torre 3000/sala 817 CEP: 20765-000, Brazil*

[53] *LAPP, Université Savoie Mont Blanc, CNRS/IN2P3, Annecy; France*

[54] *Federal University of Technology - Paraná (PPGFA/UTFPR-Curitiba), Av. Sete de Setembro, 3165, CEP 80230-901 - Curitiba - PR, Brazil*

[55] *Association of Universities for Research in Astronomy, 1331 Pennsylvania Ave NW, Washington, DC 20004*

[56] *Observatório Nacional/MCTI, R. General José Cristino 77, CEP 20921-400 Rio de Janeiro - RJ, Brazil*

[57] *Université Côte d'Azur, Observatoire de la Côte d'Azur, CNRS, Laboratoire Lagrange, Bd de l'Observatoire, CS 34229, 06304 Nice cedex 4, France*

[58] *Institute of Astrophysics, Pontificia Universidad Católica de Chile, Av. Vicuña Mackenna 4860, 7820436 Macul, Santiago, Chile*

[59] *Department of Physics, University of Auckland, Private Bag 92019, Auckland, New Zealand*

[60] *University of California, Berkeley, 501 Campbell Hall 3411, Berkeley, CA 94720, USA*

[61] *Breakthrough Listen, University of Oxford, Department of Physics, Denys Wilkinson Building, Keble Road, Oxford, OX1 3RH, UK*

[62] *SETI Institute, 339 Bernardo Ave, Suite 200, Mountain View, CA 94043, USA*

[63] *Sorbonne Université, CNRS/IN2P3, Laboratoire de Physique Nucléaire et de Hautes Energies (LPNHE), FR-75005 Paris, France*

[64] *Department of Physics and McDonnell Center for the Space Sciences, Washington University, St. Louis, MO 63130, USA*

[65] *University of Kansas, Lawrence, KS 66045*

[66] *Space Science and Technology Centre, Curtin University, GPO Box U1987, Perth WA 6845, Australia*

[67] *International Centre for Radio Astronomy Research, Curtin University, GPO Box U1987, Perth WA 6845, Australia*

[68] *Caltech/IPAC, 1200 E. California Blvd, Pasadena, CA 91125-2200*

[69] *Finnish Centre for Astronomy with ESO, University of Turku, FI-20014 Turku, Finland*

[70] *Department of Electrical and Computer Engineering, Duke University, Durham, NC 27708, USA*

[71] *INAF - Osservatorio Astronomico, Via Tiepolo 11, 34143 Trieste Italy*

[72] *Department of Physics, Case Western Reserve University, 10900 Euclid Avenue, Cleveland, OH 48106*

[73] *Astrophysics Division, National Centre for Nuclear Research, Pasteura 7, 02-093 Warsaw, Poland*

[74] *Farther Horizons, 1129 Sherman Ave, Evanston, IL 60202*

[75] *CNRS, CC-IN2P3, 21 avenue Pierre de Coubertin, CS70202, F-69627 Villeurbanne cedex, France*

[76] *LTE, Observatoire de Paris, Univ. PSL, Sorbonne Univ., Univ. Lille, LNE, CNRS, av. de l'Observatoire, 75014 Paris, France*

[77] *Asteroid Engineering Laboratory, Luleå University of Technology, Box 848, 981 28 Kiruna, Sweden*

[78] *INAF - Osservatorio Astronomico di Roma, via Frascati 33, 00078 Monte Porzio Catone (RM), Italy*

[79] *Steward Observatory and Department of Astronomy, University of Arizona, 933 N. Cherry Ave, Tucson, AZ, 85721*

[80] *Department of Astronomy, Yonsei University, 50 Yonsei-ro, Seoul 03722, Korea;* `mkjee@yonsei.ac.kr`

[81] *Department of Physics, University of California, Davis, One Shields Avenue, Davis, CA 95616, USA*

[82] *Institute of Physics, Federal University of Uberlândia, Av. João Naves de Ávila, Uberlândia, Minas Gerais CEP 38408-100, Brazil*

[83] *Laboratoire de Physique Nucléaire et de Hautes Énergies, 4 Place Jussieu, Paris, France*

[84] *Physics Department, University of California, 366 Physics North, MC 7300 Berkeley, CA 94720, USA*

[85] *Department of Physics, Duke University, Durham, NC 27708, USA144*

[86] *Kavli Institute for Particle Astrophysics and Cosmology, Stanford University, 2575 Sand Hill*

[87] *Astronomical Observatory Institute, Adam Mickiewicz University, Słoneczna 36, 60-286 Poznań, Poland*

[88] *Brookhaven National Laboratory, Upton, NY 11973, USA*

[89] *B612 Foundation Asteroid Institute, 20 Sunnyside Ave Ste F, Mill Valley, California, 94941, United States*

[90] *Department of Earth, Planetary, and Space Sciences, University of California, Los Angeles*

[91] *Instituto de Astrofisica de Canarias (IAC), C/Via Lactea s/n, 38205 La Laguna, Tenerife, Spain*

[92] *Department of Physics, University of Michigan, Ann Arbor, MI 48109, USA*

[93] *Michigan Institute for Data and AI in Society, University of Michigan, Ann Arbor, MI 48109, USA*

[94] *Division of Physics, Mathematics and Astronomy, California Institute of Technology, Pasadena, CA 91125, USA*

[95] *Center for Data Driven Discovery, California Institute of Technology, Pasadena, CA 91125, USA*

[96] *Université Marie et Louis Pasteur, CNRS, Institut UTINAM (UMR 6213), équipe Astro, F-25000 Besançon, France*

[97] *Department of Astronomy, University of Michigan, Ann Arbor, MI 48109, USA*

[98] *Université Paris-Saclay, CNRS/IN2P3, IJCLab, 91405 Orsay, France*

[99] *University of Belgrade, Faculty of Mathematics, Departmen of Astronomy, Studentski trg 16, Belgrade, Serbia*

[100] *Instituto de Astronomía y Física del Espacio. (UBA-CONICET). Int. Guiraldes S/N CABA. Argentina.*

[101] *Inter-University Centre for Astronomy and Astrophysics, Ganeshkhind, Pune, India 411007*

[102] *Allen Institute for Brain Science, 615 Westlake Ave N, Seattle, WA 98109*

[103] *School of Applied and Engineering Physics, Mohammed VI Polytechnic University, BenGuerir, 43150, Morocco.*

[104] *Instituto de Astronomía y Ciencias Planetarias, Universidad de Atacama, Copayapu 485, Copiapó, Chile*

[105] Department of Astronomy and Physics, University of Pennsylvania, 209 S. 33rd St., Philadelphia, PA 19104
[106] Longwood University, 201 High Street, Farmville, VA 23909
[107] Department of Physics and Astronomy, Purdue University, 525 Northwestern Avenue, West Lafayette, IN 47907
[108] Brigham Young University, Department of Physics and Astronomy, N283 ESC, Provo, UT 84602, USA
[109] Department of Astronomy, Yale University, 219 Prospect Street, New Haven, CT 06511, USA
[110] Johns Hopkins University Applied Physics Laboratory, 11100 Johns Hopkins Rd., Laurel, MD 20723
[111] Aix Marseille Univ, CNRS/IN2P3, CPPM, Marseille, France
[112] Science Systems and Applications, Inc, 10210 Greenbelt Rd, Lanham, MD 20706
[113] Florida Space Institute, University of Central Florida, 12354 Research Parkway, Orlando, FL, 32826, USA
[114] Space Telescope Science Institute, 3700 San Martin Drive, Baltimore, MD 21218, USA
[115] J.Sick Codes Inc., Penetanguishene, Ontario, Canada
[116] Department of Math, Physics, and Computer Science, Baker University, P.O. Box 65 Baldwin City, Kansas 66006
[117] ASTRON Netherlands Institute for Radio Astronomy, Oude Hoogeveensedijk 4, 7991 PD, Dwingeloo, The Netherlands
[118] ELTE Gothard Astrophysical Observatory, Szent Imre Herceg st. 112, H-9704 Szombathely, Hungary
[119] Department of Physics, Harvard University, 17 Oxford St., Cambridge MA 02138, USA
[120] Pittsburgh Particle Physics, Astrophysics, and Cosmology Center (PITT PACC). Physics and Astronomy Department, University of Pittsburgh, Pittsburgh, PA 15260, USA
[121] Instituto de Estudios Astrofísicos, Facultad de Ingeniería y Ciencias, Universidad Diego Portales, Santiago, Chile
[122] Center for Space Physics, Boston University, 725 Commonwealth Ave, Boston, MA 02215, USA

ABSTRACT

We report on the observation and measurement of astrometry, photometry, morphology, and activity of the interstellar object 3I/ATLAS, also designated C/2025 N1 (ATLAS), with the NSF-DOE Vera C. Rubin Observatory. The third interstellar object, comet 3I/ATLAS, was first discovered on UT 2025 July 1. Serendipitously, the Rubin Observatory collected imaging in the area of the sky inhabited by the object during regular commissioning activities. We successfully recover object detections from Rubin visits spanning UT 2025 June 21 (10 days before discovery) to UT 2025 July 7. Facilitated by Rubin's high resolution and large aperture, we report on the detection of cometary activity as early as June 21st, and observe it throughout. We measure the location and magnitude of the object on 37 Rubin images in r, i, and z bands, with typical precision of ~ 20 mas (100 mas, systematic) and ~ 10 mmag, respectively. We use these to derive improved orbit solutions, and to show there is no detectable photometric variability on hourly timescales. We derive a V-band absolute magnitude of $H_V = (13.7 \pm 0.2)$ mag, and an equivalent effective nucleus radius of $\sim (5.6 \pm 0.7)$ km. These data represent the earliest observations of this object by a large ($\gtrsim$8-meter class) telescope reported to date, and illustrate the type of measurements (and discoveries) Rubin's Legacy Survey of Space and Time (LSST) will begin to provide once operational later this year.

Keywords: Comae (271), Comet tails (274), Interstellar objects (52)

1. INTRODUCTION

1.1. *Background*

Interstellar Objects (ISOs) are small bodies detected in the solar system but not gravitationally bound to our star. They are presumed to be passing through our planetary system but having origins in exoplanetary systems in our Galaxy. Studies of these objects can reveal the bulk compositions and surface processing of extrasolar planetesimals, and the dynamical footprints of the planetary systems that ejected them (Fitzsimmons et al. 2023; Seligman & Moro-Martín 2022; Jewitt & Seligman 2023; Moro-Martín 2022). However, our knowledge of this population remains sparse, as only three have been identified: 1I/'Oumuamua (Williams et al. 2017), 2I/Borisov (Borisov et al. 2019), and now, 3I/ATLAS (Figure 1), discovered UT 2025 July 1 (S. Deen et al. 2025; Denneau et al. 2025).

The first interstellar object, 1I/'Oumuamua, discovered in October 2017, did not show any visible coma or outgassing (Meech et al. 2017; Ye et al. 2017; Jewitt

* DiRAC Post-doctoral Fellow
† LSST-DA Catalyst Postdoctoral Fellow
‡ NSF Astronomy and Astrophysics Postdoctoral Fellow
§ Author is deceased

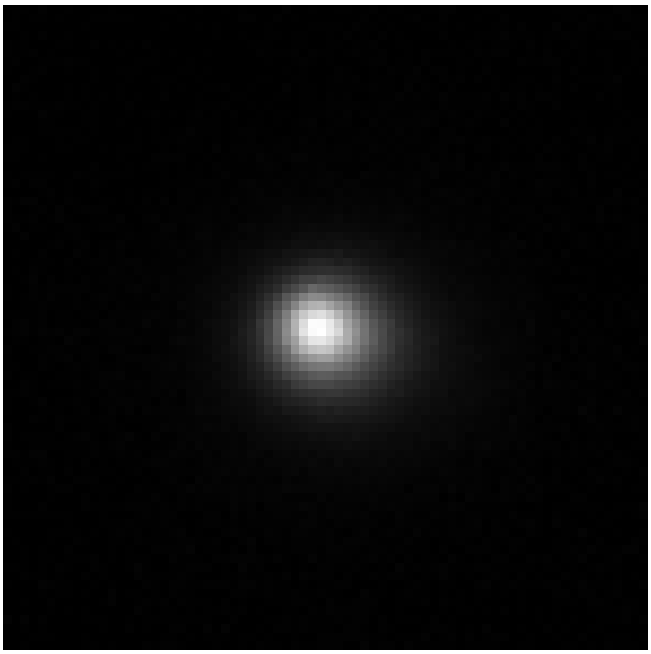


Figure 1. 3I/ATLAS minimum co-addition from UT 2025 July 3, 21×30 s r-band images acquired by NSF-DOE Vera C. Rubin Observatory. The FOV is $15'' \times 15''$, with North up and East left.

et al. 2017; Trilling et al. 2018), yet the object exhibited significant non-gravitational acceleration (Micheli et al. 2018; 'Oumuamua ISSI Team et al. 2019) and an unusually large light curve amplitude indicating an elongated or flattened, tumbling shape (Drahus et al. 2017; Knight et al. 2017; Bannister et al. 2017; Bolin et al. 2018; Fraser et al. 2018; McNeill et al. 2018; Belton et al. 2018; Mashchenko 2019). 2I/Borisov, discovered in August 2019, became the second interstellar object identified in our Solar System. In contrast to 1I/'Oumuamua's visibly inert nature, 2I/Borisov displayed a pronounced dust and gas coma, making it the first interstellar comet (Jewitt & Luu 2019; Fitzsimmons et al. 2019; Bolin et al. 2020; Ye et al. 2020; McKay et al. 2020; Guzik et al. 2020; Hui et al. 2020; Kim et al. 2020; Cremonese et al. 2020; Yang et al. 2021; Deam et al. 2025; de León et al. 2019, 2020). Unlike other inner Solar System comets, 2I/Borisov had a much higher CO/H_2O abundance ratio (Bodewits et al. 2020; Cordiner et al. 2020).

1.2. *3I/ATLAS*

The third interstellar object, 3I/ATLAS, also designated C/2025 N1 (ATLAS), was first identified on UT 2025 July 1 (Denneau et al. 2025) by the Asteroid Terrestrial-impact Last Alert System (ATLAS) (Tonry et al. 2018). It quickly became clear that the object was of interstellar origin, with an eccentricity exceeding 6[1]. Numerous follow-up observers quickly identified the presence of a faint cometary tail, establishing the object as a weakly active cometary body (e.g., Jewitt & Luu 2025; Alarcon et al. 2025; Seligman et al. 2025; Opitom et al. 2025; Bolin et al. 2025). Multi-filter imaging and spectroscopy by multiple observers (Seligman et al. 2025; Opitom et al. 2025; Champagne et al. 2025; Bolin et al. 2025; Bolin et al. 2025; Alvarez-Candal et al. 2025) indicated that the object had a moderately red spectral gradient of $S' \sim 18\%/100$ nm, at least some of which was likely due to a dust coma given the object's visible activity at the time of those observations.

Meanwhile, no gas emission was detected in Very Large Telescope (VLT)/Multi Unit Spectroscopic Explorer (MUSE) observations on UT 2025 July 3 (Opitom et al. 2025), when the object was at a heliocentric distance of $r_h = 4.47$ au (Table 2). Bolin et al. (2025) computed a non-nucleus-subtracted $A(0°)f\rho$ of 280.8 ± 3.2 cm and estimated a dust mass-loss rate of 0.1–1.0 kg s^{-1}, noting that this level of activity was comparable to that of 2I/Borisov (Prodan et al. 2024) but far exceeding that of 1I/'Oumuamua.

Nucleus measurements have also been attempted, but should be regarded with caution given the established presence of a dust coma. The strongest constraint on the nucleus size to date is likely provided by precovery observations on UT 2025 May 22 obtained by the Zwicky Transient Facility (ZTF), from which Seligman et al. (2025) derived a lower limit V-band absolute magnitude of $H_V = 12.4$ mag, corresponding to an upper limit effective radius of $r_n < 10$ km, assuming an asteroid-like albedo ($A = 0.05$). In those precovery data, ZTF measured $g'-r'$ colors that were nearly solar (Seligman et al. 2025), suggesting that the object's nucleus may not be as red as later observations, which include flux contributions from a by-then detectable coma. However, as the ZTF multi-filter observations were not simultaneous (and therefore subject to potential light curve variability) and the presence of an unresolved coma even in those earlier data cannot be ruled out, these results should be regarded as uncertain. Meanwhile, time-series observations have revealed a largely flat light curve (amplitude < 0.2 mag; e.g., Seligman et al. 2025; Champagne et al. 2025), suggesting that the object could be nearly spherical, the rotational pole could be close to the line of sight with respect to the Earth, nucleus rotational light curve variations might be damped by a nearly steady-state coma, or a combination of all of these factors. As the coma is already resolved, it is likely that

[1] https://ssd.jpl.nasa.gov/tools/sbdb_lookup.html#/?sstr=C%2F2025%20N1

the latter explanation is dominant, and the nucleus is considerably smaller than 10 km in radius.

Based on the published data from the ATLAS survey's discovery of 3I/ATLAS, Loeb (2025) notes that a $r_n \sim 10$ km implies a local number density $n_0 \sim 3 \times 10^{-4}\,\mathrm{au}^{-3}$, which would overproduce interstellar mass. To resolve this mass-budget conflict, Loeb concluded that 3I/ATLAS must either be a comet with a small nucleus ($r_n \lesssim 0.6$ km) or a rare ~ 10 km body with $n_0 \lesssim 5 \times 10^{-8}\,\mathrm{au}^{-3}$. Seligman et al. (2025) concluded that 3I/ATLAS has a number density $n_0 \sim 10^{-3}\,\mathrm{au}^{-3}$.

Hopkins et al. (2025) used *Gaia* DR3 and 3I/ATLAS's orbital arc (fit as of 2025 July 3) to show 3I/ATLAS's velocity is outside of the main moving-group structures in the Ōtautahi–Oxford ISO model, unlike those of 1I/'Oumuamua and 2I/Borisov. 3I/ATLAS has a high velocity perpendicular to the Galactic plane, creating its unusually Southern direction of approach for an ISO. They rule out any common origin with 1I/'Oumuamua or 2I/Borisov based on kinematic exclusion, and derive a broad age range, with the age for 3I/ATLAS most likely older than 7 Gyr, underscoring the large uncertainty in ISO age estimates (Hopkins et al. 2025; Marčeta & Seligman 2023); this age is supported by the subsequent ~ 3 - 11 Gyr estimate of Taylor & Seligman (2025) and the general conclusions that 3I/ATLAS is older than 1I/'Oumuamua and 2I/Borisov (Kakharov & Loeb 2025).

2. THE VERA C. RUBIN OBSERVATORY

The NSF-DOE Vera C. Rubin Observatory (Ivezić et al. 2019)[2] resides atop Cerro Pachón in Chile, hosting the 8.4 m Simonyi Survey Telescope (Stalder et al. 2024) equipped with the 3.2 gigapixel Legacy Survey of Space and Time (LSST) Camera (LSSTCam; SLAC National Accelerator Laboratory & NSF-DOE Vera C. Rubin Observatory 2025; Roodman et al. 2024), which covers a 9.6 deg^2 field of view sampled at 0.2″ per pixel to a depth of $m_r \sim 24$ with a 30 second exposure. Rubin Observatory will begin the LSST, an ambitious ten-year imaging survey of the southern sky, towards the end of 2025. Ivezić et al. (2019) provide an overview of Rubin and the LSST, including the science drivers that led to its specific configuration. During its main survey the LSST will obtain observations from near-UV to near-IR (*ugrizy* bandpasses) with approximately 30-second exposures, imaging the entire visible southern sky repeatedly every few nights. Bianco et al. (2022) provide a more detailed overview of the survey strategy.

[2] https://rubinobservatory.org

Rubin Observatory is currently in its commissioning period, although at a stage where the Science Validation (SV) has begun (see Section 6 of Claver et al. 2025). During this period, data quality and acquisition rate are variable. Summit systems, including the Active Optics System (AOS), are still being refined, and observing procedures, such as interrupts for Target of Opportunity (ToO), are still being tested. Not all data products that will be available during LSST operations are currently available. In particular, the SV survey has not yet progressed far enough to have sufficient images available to create templates for difference imaging across its footprint.

The SV survey began limited operations on June 20, 2025, running for approximately 5 hours out of the 10 hour night over approximately 1447 deg^2. This first night of the SV survey coincidentally covered the position of 3I/ATLAS – the first detection of 3I/ATLAS with Rubin. That and the following nights (UT 2025 June 21-24) provide the earliest high-resolution, deep observations of 3I/ATLAS and a unique opportunity to study its brightness and morphology at larger distances before its perihelion approach to the Sun. The SV survey continued to make serendipitous observations of 3I/ATLAS through late June and early July. Out of the 49 potential observations included in this paper, 19 of these were during the normal operation of the SV survey. Not all of the acquired images were suitable for scientific purposes; one visit (`visit_id` 2025062300417 from 2025 June 23) was taken out of focus and stars appeared as "donuts" (Figure A1). A series of 30 images on the night of 2025 July 2 between `visit_id` 2025070200479 and 2025070200508 were acquired during an alignment sequence for the AOS. The sequence was a planned part of test operations for that night, but – noticing the opportunity – the Observing Specialist shifted its location to coincide with 3I/ATLAS's position. From 2025 July 07 to 2025 July 10, 3I/ATLAS was within Rubin's Moon avoidance zone.

3. 3I/ATLAS SEARCH AND DETECTIONS IN RUBIN COMMISSIONING DATA

3.1. *Image Search*

We initially derived interpolated and extrapolated 3I/ATLAS positions from the ephemeris provided by the JPL Scout service (Farnocchia et al. 2016), once for the date/time of every LSSTCam and LSST Commissioning Camera (LSSTComCam; SLAC National Accelerator Laboratory & NSF-DOE Vera C. Rubin Observatory 2024) visit from the Rubin `exposure` table, which includes engineering images in addition to science exposures. For each visit, we checked to see if 3I/ATLAS

was within $\sim 9^\circ$ of any of the pointing (boresight) center on-sky coordinates. In addition, we used the available astrometric data on Scout before 2025 July 2 to re-fit the orbit using the orbit fitting software LAYUP[3], and these solutions were used to propagate 3I/ATLAS's ephemerides to all LSSTCam visits using the survey simulation software SORCHA[4] (Merritt et al. 2025; Holman et al. 2025). The use of these two methodologies ensured that we were able to extract all possible images of 3I/ATLAS in this preliminary LSST data.

Following the methods outlined in Chandler et al. (2024), we extracted cutouts of each available calibrated image (`preliminary_visit_image`) and, when calibrated data was not available, raw images. We reprojected with North up and East left to facilitate tail identification and comparison with anti-solar and anti-motion vectors (as projected on the sky), the most likely directions for tails to be observed though, for 3I/ATLAS, the tail was more sunward at the time of discovery (Opitom et al. 2025 and Section 4.9.3). Subsequently, we extracted cutouts of 3I/ATLAS based on the positions produced by our own measurement-derived orbit computations of 3I/ATLAS (Section 4.5). For images unavailable in calibrated format, we manually reprocessed the data with the LSST software pipelines.

For the special case of the "donut" image (UT 2025 June 24; Figure A1), we worked exclusively with the raw data. To identify 3I/ATLAS here, we first queried the Gaia DR3 catalog (Gaia Collaboration et al. 2023) via `AstroQuery` (Ginsburg et al. 2019) and the Vizier catalog tool (Ochsenbein et al. 2000) and overplotted the positions of the stars. We manually applied an (x, y) translational offset to account for deviations in the preliminary World Coordinate System (WCS) supplied with the raw image data. We next overplotted an equally offset position for 3I/ATLAS, provided by the JPL Horizons ephemeris service (Giorgini et al. 1996). Virtually all sources in the frame match known Gaia DR3 sources, with the exception of the source that appeared in the calculated position for 3I/ATLAS.

For the case of UT 2025 June 30 (Figures 2d and 2e), we followed a similar procedure to that used for the UT 2025 June 24 donuts image. In this case, we overplotted the known Gaia DR3 stars for both images; in the second image, 3I/ATLAS is identifiable adjacent to the saturated star. We also reprocessed the images with the pipeline, disabling the saturation correction. The list of images is included in Table 1. The log of aspect geometry for the days with detections is summarized in Table 2.

[3] https://github.com/Smithsonian/layup
[4] https://sorcha.readthedocs.io/

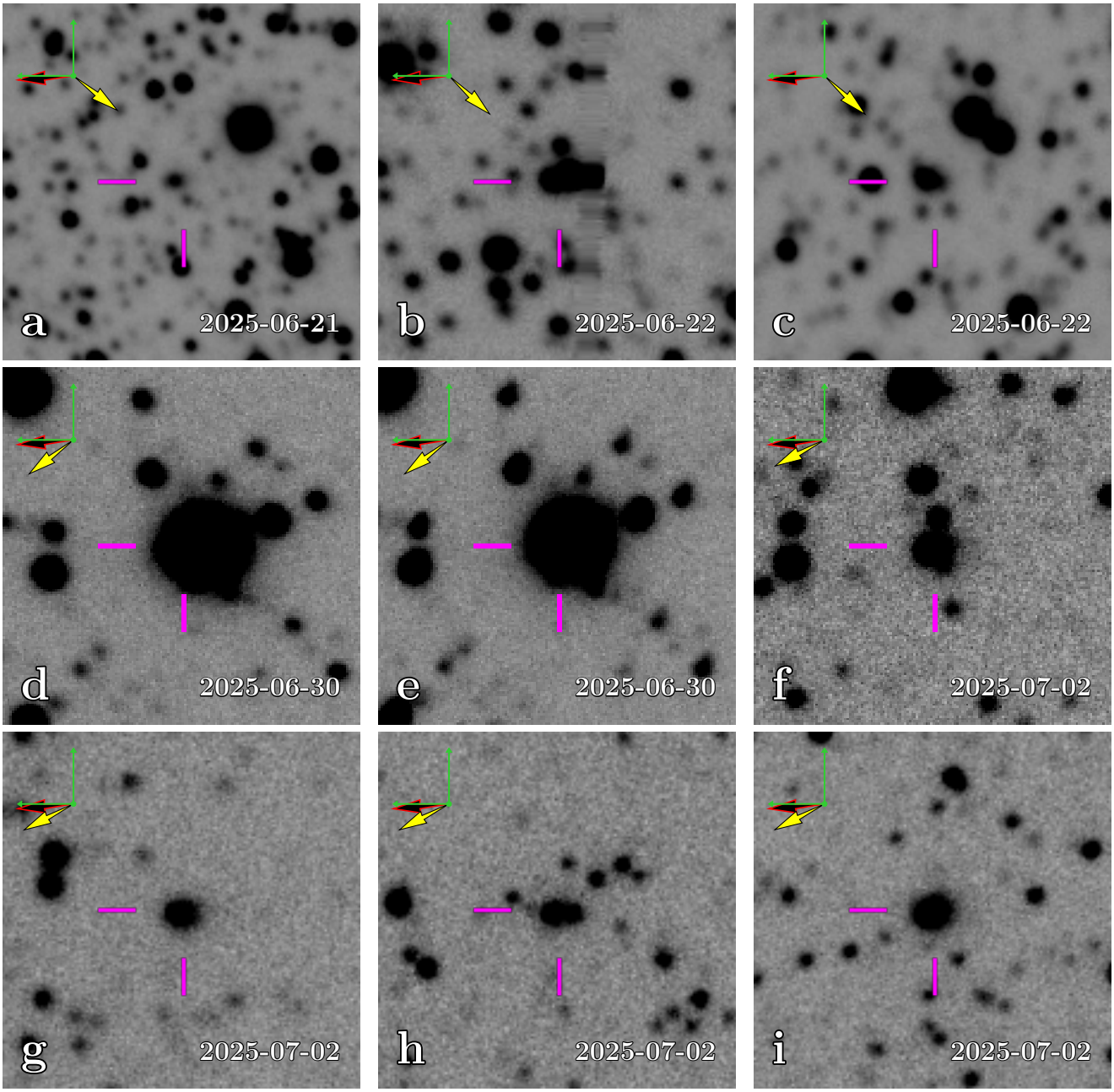


Figure 2. Gallery of serendipitous observations of 3I/ATLAS from the NSF-DOE Vera C. Rubin Observatory (site code X05). All images are $30'' \times 30''$ and have been reprojected so that North appears up, and East to the left. The anti-solar (yellow, black-outlined arrow) and anti-motion (black, red-outlined arrow) directions are indicated. All dates and times are TAI. **(a)** 2025 June 21 08:11:32. **(b)** 2025 June 22 02:32:47. An area of roughly vertical saturation masking can be seen near the center of the frame; 3I/ATLAS is not within the masking, but the nearby blended star is. **(c)** 2025 June 22 03:07:49. **(d)** 2025 June 30 02:25:46. 3I/ATLAS is in front of a saturated star. **(e)** 2025 June 30 02:26:26. 3I/ATLAS is adjacent to the saturated star at the center. **(f)** 2025 July 02 00:44:25. **(g)** 2025 July 02 01:20:33. **(h)** 2025 July 02 02:31:16. **(i)** 2025 July 02 03:33:02.

Table 1. Table of Observations

Row	Date Midpoint (TAI)	Filter	Visit ID	Chip	Flags	Meas. RA (deg)	Meas. Dec (deg)	Mag (mag)	Mag Err (mag)	r (au)	Delta (au)	Elong (deg)	Phase (deg)	Sky Vel (″/min)	Sky PA (deg)
1	2025-06-21 08:11:32.665	z	2025062000620	104	-					4.839	3.830	172.22	1.63	1.021	270.25
2	2025-06-22 02:32:47.429	g	2025062100383	38	- BA					4.813	3.803	173.02	1.47	1.037	270.11
3	2025-06-22 03:07:49.625	r	2025062100431	38	- B					4.813	3.802	173.05	1.46	1.038	270.13
4	2025-06-24 03:07:46.213	i	2025062300417	77	-D BA					4.746	3.733	174.77	1.12	1.079	270.33
5	2025-06-30 02:25:46.504	i	2025062900392	172	- SBA					4.546	3.536	172.45	1.68	1.199	270.96
6	2025-06-30 02:26:26.639	i	2025062900393	9	- BA					4.546	3.536	172.45	1.68	1.199	270.97
7	2025-07-02 00:44:25.734	i	2025070100200	119	- B	271.44780021	-18.68489767	18.17	0.011	4.482	3.477	170.12	2.23	1.235	271.16
8	2025-07-02 01:20:33.931	z	2025070100248	119	+	271.43468765	-18.68462292	18.03	0.013	4.481	3.476	170.09	2.24	1.236	271.18
9	2025-07-02 02:31:16.539	z	2025070100350	119	- B					4.479	3.475	170.02	2.25	1.239	271.22
10	2025-07-02 03:33:02.401	i	2025070100399	119	+	271.38661792	-18.68351107	18.24	0.010	4.478	3.473	169.97	2.27	1.240	271.26
11	2025-07-03 01:53:12.949	i	2025070200188	6	- B	270.89965982	-18.67140964	18.13	0.010	4.447	3.445	168.76	2.56	1.257	271.32
12	2025-07-03 03:03:56.766	z	2025070200274	6	+	270.87355655	-18.67073595		0.010	4.445	3.444	168.69	2.57	1.259	271.37
13	2025-07-03 06:25:00.588	r	2025070200479	94	+ B	270.79925893	-18.66879115	18.28	0.010	4.441	3.440	168.50	2.62	1.261	271.51
14	2025-07-03 06:27:17.374	r	2025070200480	94	+ B	270.79843677	-18.6687389	18.29	0.010	4.440	3.440	168.50	2.62	1.261	271.51
15	2025-07-03 06:32:03.644	r	2025070200481	94	+ B	270.79665019	-18.66872252	18.37	0.010	4.440	3.439	168.50	2.62	1.261	271.51
16	2025-07-03 06:36:22.936	r	2025070200482	94	+ B	270.7950661	-18.66867034	18.41	0.010	4.440	3.439	168.49	2.62	1.261	271.51
17	2025-07-03 06:48:53.518	r	2025070200483	94	+	270.79044054	-18.66854942	18.37	0.010	4.440	3.439	168.48	2.62	1.260	271.52
18	2025-07-03 06:49:27.817	r	2025070200484	94	+	270.79022012	-18.66854323	18.33	0.010	4.440	3.439	168.48	2.62	1.260	271.52
19	2025-07-03 06:50:17.900	r	2025070200485	94	+	270.78991584	-18.66854239	18.42	0.010	4.440	3.439	168.48	2.62	1.260	271.52
20	2025-07-03 06:50:52.210	r	2025070200486	94	+	270.78970868	-18.66853107	18.44	0.010	4.440	3.439	168.48	2.62	1.260	271.52
21	2025-07-03 06:51:47.398	r	2025070200487	94	+ B	270.78935403	-18.66851411	18.39	0.010	4.440	3.439	168.48	2.62	1.260	271.52
22	2025-07-03 06:52:21.699	r	2025070200488	94	+ B	270.78914766	-18.66851621	18.45	0.010	4.440	3.439	168.48	2.62	1.260	271.52
23	2025-07-03 06:53:16.948	r	2025070200489	94	+ B	270.78879974	-18.66850929	18.43	0.010	4.440	3.439	168.48	2.62	1.260	271.52
24	2025-07-03 06:53:51.225	r	2025070200490	94	+	270.78859561	-18.66849454	18.45	0.010	4.440	3.439	168.48	2.62	1.260	271.52
25	2025-07-03 06:54:40.905	r	2025070200491	94	+	270.78828964	-18.66847775	18.43	0.010	4.440	3.439	168.48	2.62	1.260	271.52
26	2025-07-03 06:55:15.188	r	2025070200492	94	+ B	270.78808866	-18.66847692	18.45	0.010	4.440	3.439	168.47	2.62	1.260	271.52
27	2025-07-03 06:58:56.345	r	2025070200493	94	- B	270.78671566	-18.66846525	18.41	0.010	4.440	3.439	168.47	2.62	1.260	271.53
28	2025-07-03 06:59:30.625	r	2025070200494	94	+ B	270.7865084	-18.66842505	18.38	0.010	4.440	3.439	168.47	2.62	1.260	271.53

Table 1 *continued*

Table 1 *(continued)*

Row	Date Midpoint (TAI)	Filter	Visit ID	Chip	Flags	Meas. RA (deg)	Meas. Dec (deg)	Mag (mag)	Mag Err (mag)	r (au)	Delta (au)	Elong (deg)	Phase (deg)	Sky Vel (″/min)	Sky PA (deg)
29	2025-07-03 07:00:20.326	r	2025070200495	94	+ B	270.78620235	-18.66843063	18.37	0.010	4.440	3.439	168.47	2.62	1.260	271.53
30	2025-07-03 07:00:54.818	r	2025070200496	94	+ B	270.78599054	-18.66842558	18.41	0.010	4.440	3.439	168.47	2.62	1.260	271.53
31	2025-07-03 07:01:46.238	r	2025070200497	94	+	270.78567121	-18.66842246	18.42	0.010	4.440	3.439	168.47	2.62	1.260	271.53
32	2025-07-03 07:02:20.680	r	2025070200498	94	+ B	270.78546068	-18.66841908	18.44	0.010	4.440	3.439	168.47	2.62	1.260	271.53
33	2025-07-03 07:07:48.633	r	2025070200499	94	+	270.78344117	-18.66838093	18.4	0.010	4.440	3.439	168.46	2.63	1.260	271.53
34	2025-07-03 07:08:22.937	r	2025070200500	94	+	270.78322561	-18.66835954	18.37	0.010	4.440	3.439	168.46	2.63	1.260	271.53
35	2025-07-03 07:09:07.240	r	2025070200501	94	+ B	270.78295107	-18.66835181	18.39	0.010	4.439	3.439	168.46	2.63	1.260	271.53
36	2025-07-03 07:09:41.513	r	2025070200502	94	+	270.78273404	-18.66834361	18.36	0.010	4.439	3.439	168.46	2.63	1.260	271.53
37	2025-07-03 07:10:31.380	r	2025070200503	94	+	270.78243615	-18.66833889	18.4	0.010	4.439	3.439	168.46	2.63	1.260	271.53
38	2025-07-03 07:11:05.673	r	2025070200504	94	+	270.78222737	-18.66833238	18.39	0.010	4.439	3.439	168.46	2.63	1.260	271.53
39	2025-07-03 07:11:55.955	r	2025070200505	94	+	270.78190417	-18.66831809	18.4	0.010	4.439	3.439	168.46	2.63	1.260	271.53
40	2025-07-03 07:12:30.249	r	2025070200506	94	+	270.78170379	-18.66830862	18.44	0.010	4.439	3.439	168.46	2.63	1.260	271.53
41	2025-07-03 07:13:19.464	r	2025070200507	94	+	270.78138618	-18.66829705	18.37	0.010	4.439	3.439	168.46	2.63	1.260	271.53
42	2025-07-03 07:13:53.753	r	2025070200508	94	+	270.78116945	-18.66827825	18.35	0.010	4.439	3.439	168.46	2.63	1.260	271.53
43	2025-07-04 06:36:15.986	r	2025070300497	98	- BA	270.26213533	-18.65412757	19.02	0.005	4.407	3.410	167.14	2.94	1.280	271.65
44	2025-07-05 01:23:40.236	y	2025070400162	137	-					4.381	3.387	166.07	3.20	1.295	271.58
45	2025-07-05 01:23:40.236	y	2025070400162	144	-					4.381	3.387	166.07	3.20	1.295	271.58
46	2025-07-05 01:56:38.176	y	2025070400210	137	-					4.380	3.387	166.04	3.21	1.296	271.59
47	2025-07-05 01:56:38.176	y	2025070400210	144	-					4.380	3.387	166.04	3.21	1.296	271.59
48	2025-07-06 23:34:15.015	y	2025070600033	41	-					4.317	3.333	163.37	3.87	1.328	271.81
49	2025-07-06 23:53:08.910	y	2025070600062	41	+					4.316	3.333	163.35	3.87	1.329	271.81
50	2025-07-07 00:12:48.852	y	2025070600092	41	-					4.316	3.332	163.33	3.88	1.330	271.82
51	2025-07-07 00:44:03.262	y	2025070600140	41	- B					4.315	3.332	163.30	3.88	1.332	271.83

NOTE—Table flags: + indicates images used in photometric and astrometric analysis; - indicates excluded images. B for blended, S for saturated, A for image artifact, D for out-of-focus or donuts.

Table 2. Viewing geometry of 3I/ATLAS for the dates of observations. R: solar distance, Δ: heliocentric distance, E: solar elongation, α: solar phase angle; the last two columns show the velocity and position angle (PA) of the apparent motion on the sky

Date (0h UTC)	R (au)	Δ (au)	E (°)	α (°)	Sky motion ″/min	PA_{Motion} (°)
2025-Jun-21	4.850	3.842	171.8	1.70	1.009	269.9
2025-Jun-22	4.817	3.807	172.9	1.49	1.029	270.0
2025-Jun-24	4.750	3.737	174.7	1.13	1.070	270.2
2025-Jun-30	4.549	3.539	172.6	1.65	1.192	270.9
2025-Jul-02	4.483	3.478	170.2	2.22	1.232	271.1
2025-Jul-03	4.449	3.448	168.9	2.53	1.252	271.3
2025-Jul-04	4.416	3.418	167.5	2.85	1.271	271.4
2025-Jul-05	4.383	3.389	166.2	3.18	1.291	271.5
2025-Jul-06	4.350	3.360	164.8	3.52	1.310	271.7
2025-Jul-07	4.316	3.332	163.3	3.87	1.330	271.8

In all cases, we produced comparison images showing the same area of sky but at a time when 3I/ATLAS would not have been present. This allowed us to verify the correct identification of the object in each image where a candidate detection was found.

3.1.1. *3I/ATLAS detections*

We identified 12 potential serendipitous archival SV observations of 3I/ATLAS in Rubin metadata. Ten images appeared in science frames on imaging detectors, nine during nominal science exposures (Figure 1), and two UT 2025 June 1 exposures where 3I/ATLAS was on guiding detectors, but both were outside the area read out from the camera chip. An additional 30 images (Figure 3 gallery, Figure 1 image stack) were acquired on UT 2025 July 3, during camera calibration procedures, and further images were acquired in passing over the following few days (Figure 4).

We found nine science images that contained 3I/ATLAS within detector bounds. One image (visit/detector 2025062300417/77; Figure A1) was unintentionally out of focus due to an AOS issue; while 3I/ATLAS is detectable, it is significantly blended with a background source and did not immediately yield useful astrometry, photometry, or evidence of activity in the form of a tail or coma. In the two images (visit/detectors 2025062900392/172, 2025062900393/9), from UT 2025 June 30, 3I/ATLAS appears to move across a bright star that saturated the detectors. However, in the visit/detector 2025062900392/172, the object is separated enough to be distinguished from the brighter star; this image, however, suffers from significant blending.

On UT 2025 July 3, Rubin Observatory acquired an additional series of 30 s images in r-band (Figure 3) during telescope calibration (engineering time). Consequently, the majority of the data were acquired as "acquisition" (non-science) frames. Nevertheless, the object is clearly visible, and the majority of images were usable for our analyses.

Additional images of 3I/ATLAS were acquired over the next week, some as part of ToO testing. The Moon was within 30° for several of these nights, preventing observations entirely (ToO or otherwise). Images that were acquired are included in Figure 4.

4. ANALYSIS AND RESULTS

4.1. *Rubin data analysis pipelines*

Rubin's observing facilities are designed to be supported by a largely automated data management system (Jurić et al. 2017). Once the LSST survey begins in late 2025, products enabling Solar System science, including moving object detection, image differencing, astrometry, photometry, and morphological classification will be automatically available on minute-to-daily timescales. For details, see the LSST Data Products Definition Document (DPDD; Jurić et al. 2023) or a summary by Graham (2022).

At the time of 3I/ATLAS's discovery, only a portion of this system has been deployed and verified. This includes the data acquisition and storage system (allowing Rubin to take and store the images and image metadata), an automated "nightly validation" pipeline supporting daily data reduction for quality assurance purposes (including instrumental signature removal, WCS determination, and detection of isolated bright ($> 20\sigma$) sources). Calibration production pipelines (e.g., for generation and application of biases, darks, flats, etc.) have been commissioned as well. While Rubin's solar system pipelines have recently been demonstrated on Rubin First Look[5] observations, they was not yet active when 3I/ATLAS was discovered as it was too early into the SV survey for sufficient data to be available to enable image differencing and moving object detection.

For this reason, much of the analysis presented in this section has been done using custom pipeline runs, custom configurations, with occasional custom-written software to backfill for features not yet commissioned or unavailable for other reasons at the time of 3I/ATLAS's appearance. In particular, all of our analysis was conducted on science images (rather than difference images)

[5] https://rubinobservatory.org/news/rubin-first-look

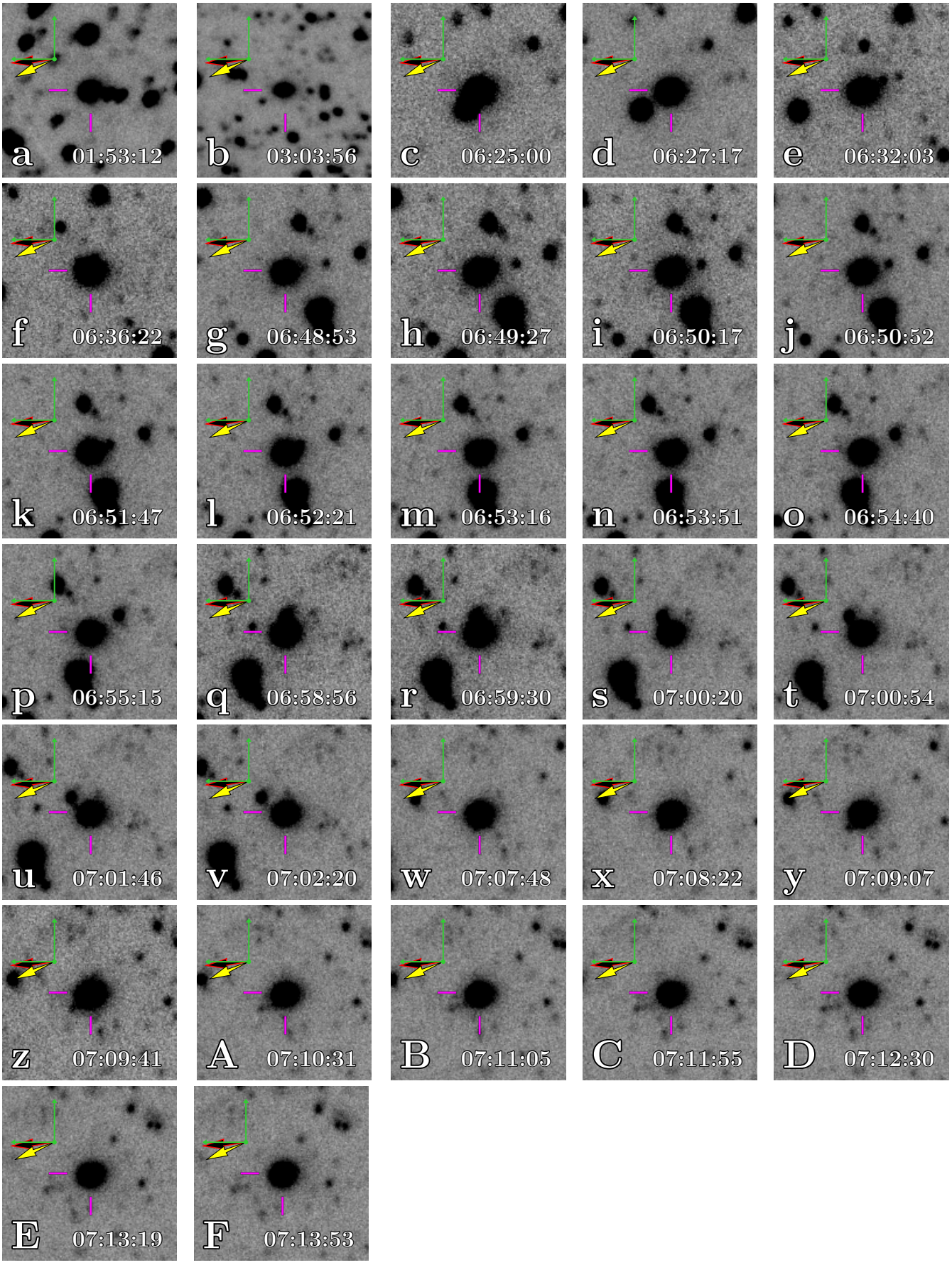


Figure 3. 3I/ATLAS imaged on UT 2025 July 3 by the NSF-DOE Vera C. Rubin Observatory as a part of commissioning. All images are 30 s r-band exposures with North up, East left, and the anti-solar $-\odot$ and anti-motion $-v$ vectors shown inset at the top-left. Exposure midpoints (TAI ISO) are overplotted.

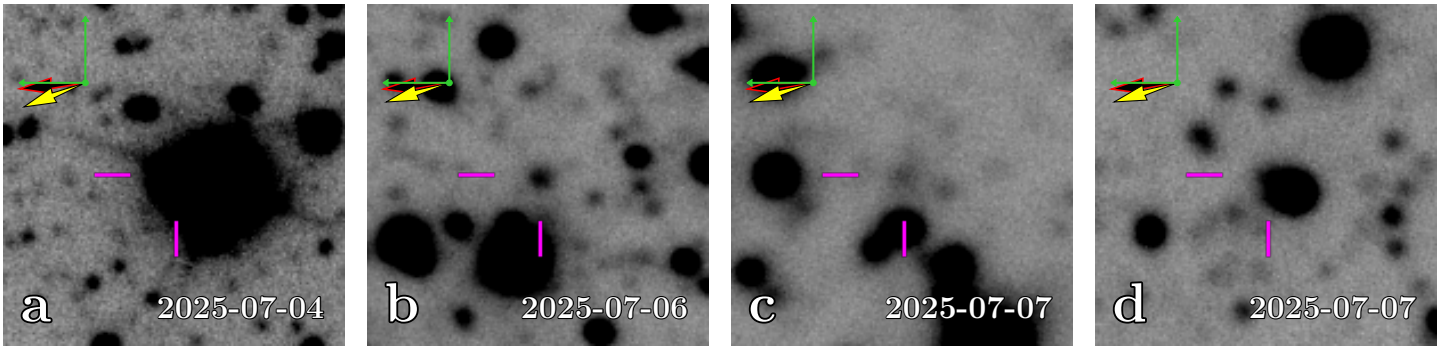


Figure 4. 3I/ATLAS (center, indicated) observations after UT 2025 July 3. North is up, East left, with the anti-solar (yellow arrow) and anti-motion (black arrow with red outline) shown as in 3.

and relied on the Rubin deblender (Melchior et al. 2018) to mitigate the confusion in crowded regions.

We therefore caution that while the *results and performance* presented in this section are expected to carry over to LSST, the *way in which these reductions and analyses were made* has been highly customized, manual, and unrepresentative of how we expect the system to function once LSST commences. In particular, elements such as object identification, detection, astrometric, and photometric measurements will all be fully automated, operate on image differences, and be conducted within minutes of observation. Further details on the LSST algorithms and pipelines can be found in Rubin Observatory Science Pipelines Developers (2025) and Bosch et al. (2018). Their present performance on LSSTComCam data, which is similar to LSSTCam but smaller in scale, is summarized in Vera C. Rubin Observatory (2025).

4.2. *Image reductions of images with 3I/ATLAS*

We use the LSST pipelines for initial pixel-level data processing. As the location of 3I/ATLAS is sufficiently well constrained, we only reduce the images for the 4k × 4k CCD detector where the object is expected to be rather than the entire 188 array active in a typical commissioning visit.

Initial reduction removes the instrument signatures (flats, darks, biases) from the raw images, fits and removes the sky background, computes the WCS solution, and photometrically calibrates the image. The WCS fits are performed relative to Gaia DR3 catalog, while photometry is calibrated with relation to PanSTARRS. We also run a special `SingleFrameDetectAndMeasure` LSST pipeline task to detect, deblend, and measure all sources found at 5σ or greater significance. As the fields in which 3I/ATLAS currently reside are fairly crowded, this task fails to converge for 15 of the images[6]. When successful, the measurements of detected sources include both astrometry (centroids) and photometry (both point spread function (PSF) and aperture fluxes). An example of a successful processing run, including the appearance of a deblended source footprint, is shown in Figure 5.

As the last step, smaller subsections 600 × 600 pixels (2 × 2 arcmin) of the resulting images are cut out and stored as FITS files. This enables easier subsequent analyses of 3I/ATLAS morphology.

[6] The typical failure mode is due to too large blends because of numerous overlapping sources. This is a software element that has not yet been fully tuned at this stage of Rubin commissioning.

4.3. *Astrometric measurement routines*

As the Rubin science pipelines stack has not yet been tuned for analyses of crowded fields, we've written a small custom centroid and magnitude extractor to specifically handle the case of 3I/ATLAS. Our code derives the positions by extracting cutouts of 30×30 pixels centered at the nominal position of an object and obtaining windowed centroid measurements (`XWIN` and `YWIN`) following a procedure analogous to that of the SOURCE EXTRACTOR (Bertin & Arnouts 1996) package. These are then propagated to celestial coordinates using the full image WCS fitted by the LSST pipelines.

To validate our measurement code, in addition to 3I/ATLAS, we also apply it to stars present in images where the Rubin detection and measurement task successfully obtained the solution, as well as known asteroids (in all images). The results are presented in Figure 6. The star centroids are in excellent agreement with the LSST stack measurements, showing differences less than 5 mas per coordinate. For asteroids, the median difference compared to JPL Horizons-computed ephemerides is on the order of 1σ, with an overall systematic offset of −20 mas in R.A. and −34 mas in Dec.

4.4. *Astrometry of 3I/ATLAS*

The astrometry of 3I/ATLAS, performed in images where the object was sufficiently well deblended using the custom code described in Section 4.3, is presented in Table 1.

We compare our measured position to JPL Horizons ephemerides (obtained as of July 14$^{\text{th}}$, 2025), noting a +113 mas residual in R.A. and −80 mas in Dec. While typically R.A. offsets can be attributed to errors in the timing for moving objects, and effects such as Differential Chromatic Refraction (DCR) can cause shifts in both R.A. and Dec, our analysis does not show similarly prominent biases when comparing the offset between 3I/ATLAS and the other asteroids. The systematic shift is also present on the subset of images successfully measured with the LSST Science Pipelines, whose performance has been extensively tested as part of the LSST Data Preview 1 (DP1) release (Vera C. Rubin Observatory 2025). In particular, DP1 demonstrated that the LSST Commissioning Camera achieved residuals of order 5 mas for high-signal to noise ratio (SNR) sources, consistent with the limits of atmospheric turbulence; a similar performance is expected here for LSSTCam.

4.5. *Orbit Fits of 3I/ATLAS*

To assess the impact of our astrometric measurements of 3I/ATLAS, we fit a new orbit solution using all available astrometry up to 2025 July 13 and perform a resid-

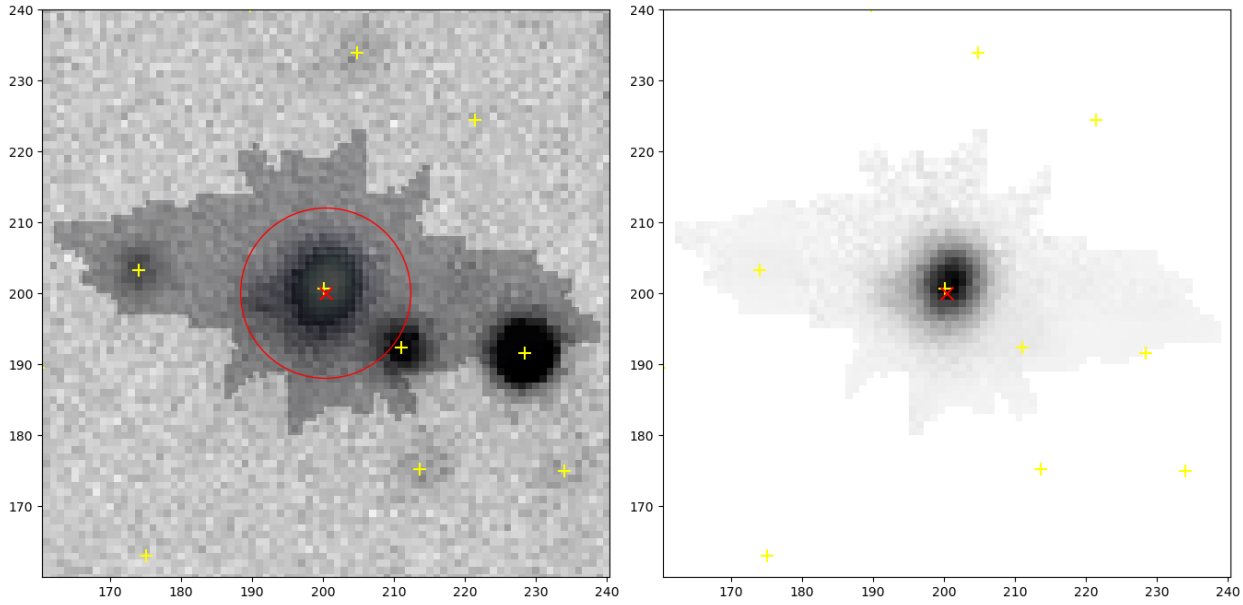


Figure 5. On the left is a cutout from a crowded field (`visit_id=2025070100200`) centered on 3I/ATLAS. The red ring represents the LSST Science Pipeline's aperture photometry radius (see Section 4.7). In the image, 3I/ATLAS is seen nestled between four sources (two to the left, two to the right). The brighter three (one to the left, and two to the right) have been detected as separate and deblended (marked with yellow plus symbols). The fourth source (just to the left of 3I/ATLAS, and inside the red ring) has not. The resulting *footprint* – a set of pixels deemed by the deblender to contain 3I/ATLAS's flux – is shown on the right. The deblender successfully removed the flux belonging to the three detected stars, preventing major biases in photometry and astrometry. However, the flux due to the fainter undetected star is still present. This illustrates both the power and caveats in deblender applications: while the worst effects of crowding are mitigated, some low-level residual flux due to faint blended sources likely remains.

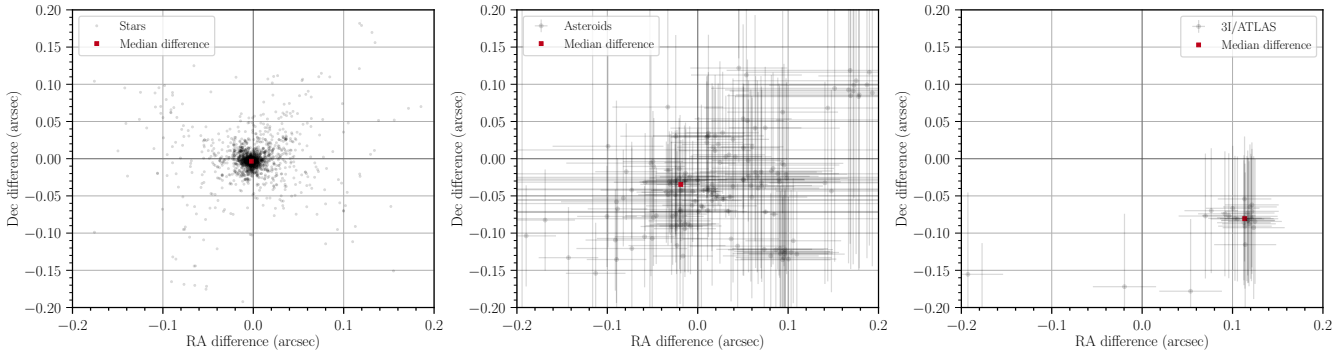


Figure 6. The three panels show the positional residuals between our windowed centroid measurements and a reference measurement for stars (left, using the LSST Science Pipelines as reference), asteroids (center, using JPL Horizons as a reference), and 3I/ATLAS (right, again using JPL Horizons). In each panel, the black points represent individual measurements, and the red square represents the median value per coordinate. For cases where JPL Horizons is the reference, we also present their uncertainties (1-σ), whereas the centroid-derived uncertainties are subdominant, due to the high-SNR of these measurements. In 3I/ATLAS's panel, the cluster of points near the median is from the 2025 July 2 images.

ual analysis using the Gauss-Radau Small-body Simulator (GRSS) (Makadia et al. 2025). GRSS is a user-friendly, open-source Python package with a C++ binding for high precision propagation and orbit fitting of small bodies in the Solar System. Astrometric measurements of asteroids by other observatories are commonly weighted according to the Vereš et al. (2017) scheme, and astrometry catalogs are debiased as suggested in Eggl et al. (2020). However, since 3I/ATLAS shows signs of cometary activity, an alternative weighting scheme has been applied, where all astrometry, including Rubin astrometry, was weighted at 1″ (likely higher than the actual astrometric performance of the telescope). These results are presented in Figure 8. As

before, we see a tight clustering of the Rubin astrometry, suggesting that Rubin will likely live up to its promised astrometric precision. We note, however, that the same bias seen before persists in this new orbit solution, with the median Rubin offset being +63 mas in R.A. and −111 mas in Dec. It is worth noting that the offset in R.A. can be reduced once observations with time biases are removed from the fit as illustrated in Figures 8 and 9. No evidence for significant non-gravitational acceleration has been found so far. The measurements indicate goodness of fit residuals $\chi \leq 1$ (see Figure 8), indicating a successful if conservative fit. We have also verified these results using Layup and the Minor Planet Center (MPC) orbit fitting software. The corresponding orbital elements and covariances are presented in Table B1.

4.6. *Understanding the origin of the observed systematic astrometric bias*

The small but detectable systematic offset relative to contemporaneous Horizons-derived ephemerides calls for an explanation. One possibility is that the centroid measurement includes excess flux due to the comet's morphology shifting its photocenter. The orbit for 3I/ATLAS, like that of most other recently discovered objects of similar brightness, is based on a heterogeneous set of measurements from observatories around the globe — hence, it is difficult to assess the significance of the median offset seen in the Rubin astrometry. If we assume this median offset is significant, one possible explanation for it could be the asymmetry of the coma (not clearly distinguishable at present from the beginning of the tail). In the 2025 July 2 observations from which most of the Rubin astrometry comes, the asymmetry consists of an extension towards the west-northwest, PA $\sim$ 290°; see Figure 7. Astrometric measurements will tend to be offset in this direction relative to the true position of the nucleus — and the offset will be greater for telescopes with larger pixels and poorer angular resolution, since a larger centroiding aperture will include more of the coma. Since Rubin has smaller pixels and better angular resolution than the smaller telescopes that have produced most of the measurements so far, we expect Rubin residuals to be in the opposite direction: PA $\sim$ 110°. The actual median offset, +63 mas in R.A. and -111 mas in Dec, corresponds to PA 151°. This agrees only roughly with the expected value of 110° — but no more than rough agreement was to be expected given the uncertainties involved. Hence, we find it plausible — though not conclusively demonstrated — that the median offset seen in Rubin astrometry arises from the fact that Rubin measurements are *less affected* than most by the asymmetrical coma of 3I/ATLAS.

To further investigate this claim, we also reproduce this analysis on data reported to the Minor Planet Center taken with the Dark Energy Camera (DECam, Flaugher et al. 2015), which has a similar pixel scale and astrometric performance to Rubin. We see a similar bias (+7 mas in R.A. and −84 mas in Dec) across 85 observations spanning from 2025 July 3 to 2025 July 8, also shown in Figure 8. The results of a more aggressive outlier rejection and weighting scheme (579 rejections) are presented in Table B2 as well as Figure 9. Here, Rubin astrometry was weighted at 250 mas. In this case, normalized post-fit residual root-mean-square (RMS) decreases from 0.38 arcsec to 0.27 arcsec, and the remaining bias of Rubin data becomes 9 mas RA cos(Dec) and −66 mas Dec.

Thus, it is possible that this astrometric offset is due to the extended nature of 3I/ATLAS and not a Rubin-specific instrument-related issue. However, we cannot fully exclude the latter. We therefore advise users to approach these measurements with caution if precision better than $\sim$ 100 mas is required. Work is ongoing to pin down and explain the exact source of this (small, but non-negligible) bias.

4.7. *Photometric Analysis*

We measure and report both aperture (fixed at 12 pixels or 2.″4) and PSF magnitudes measured by the LSST pipelines. As part of the image processing, the LSST stack attempts to deblend sources using the Scarlet Lite algorithm, based on Scarlet (Melchior et al. 2018), thus mitigating to an extent the effects of blending in crowded fields (we verify this assumption further below). To the computed errors, we also add in quadrature, a 10 mmag noise floor for the photometric measurements, the design requirement for Rubin (Ivezić et al. 2019). We note that this is a conservative estimate, as photometric performance of 5 mmag has already been demonstrated with the LSST ComCam (Vera C. Rubin Observatory 2025).

The long sequence of observations taken on UT 2025 July 3 (local observing night of 2025 July 2) gave us a unique opportunity to measure the variability of 3I/ATLAS on approximately minute timescales. We apply the Bayesian methodology of Bernardinelli et al. (2023) to both the PSF fluxes as well as the fluxes derived at a fixed aperture of 12 pixels. We assume every measurement at time i has a flux measurement $f_i = \langle f \rangle [1 + A h(\phi_i)]$, where $\langle f \rangle$ is the object's mean flux, A is its light curve semi-amplitude, and $h(\phi)$ is a time-varying function with phase $0 \leq \phi \leq 1$. We marginalize

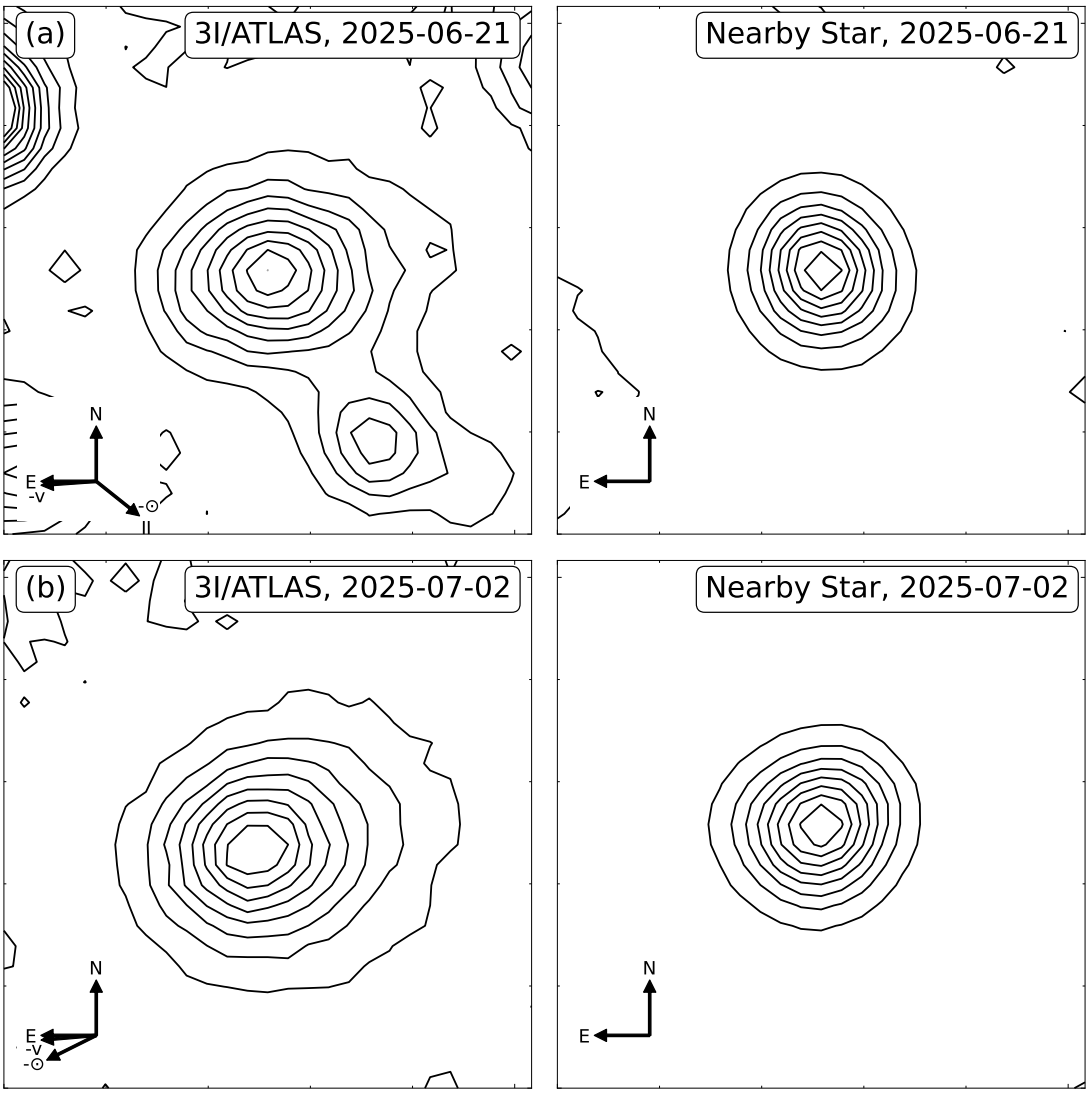


Figure 7. Contour plots (using 10 logarithmically-spaced contour levels ranging from the peak value of each image to the average background level in each image) of LSST images of 3I/ATLAS (left panel) and a nearby (within 1 arcmin of the target) reference field star from the same image (right) from (a) UT 2025 June 21 and (b) UT 2025 July 2, centered on the target. The FOV of each panel is $5'' \times 5''$. North (N), East (E), and the position angles of the anti-solar vector ($-\odot$) and negative heliocentric velocity vector ($-v$) as projected on the sky are indicated as labeled.

over ϕ for each visit, thus assuming that the object is seen at a random point of its light curve, which, for simplicity, we use $h(\phi) = \sin(2\pi\phi)$. In practice, this procedure yields a statistically rigorous Monte Carlo sampling of the probability distribution of the object's mean flux and its variability without detailed modeling of its light curve (*e.g.*, such as phase folding or shape modeling). We present the results of this analysis in the bottom panel of Figure 10. Our photometry is consistent with A on the order of 4%. This means that we can exclude variations bigger than ≈ 0.1 mag in timescales of under an hour. Incidentally, this also demonstrates good photometric stability of the Rubin system even in such a crowded field and for a moving source.

We end with a word of caution regarding deriving even lower-level variability or a light curve period from the photometry presented here. Despite our efforts at deblending, these measurements are still likely to be contaminated (at some unquantified level) by the presence of background stars, and signals from 3I/ATLAS passing on top of stars may still be present in its light curve.

While techniques such as difference imaging (Alard & Lupton 1998; Zackay et al. 2016; Sedaghat & Mahabal 2018) would be ideal to extract the photometry of this object, at this time there are few visits in each of these fields (including those with the object). Because of that, high quality templates are harder to construct and might not yield image differences that improve on mea-

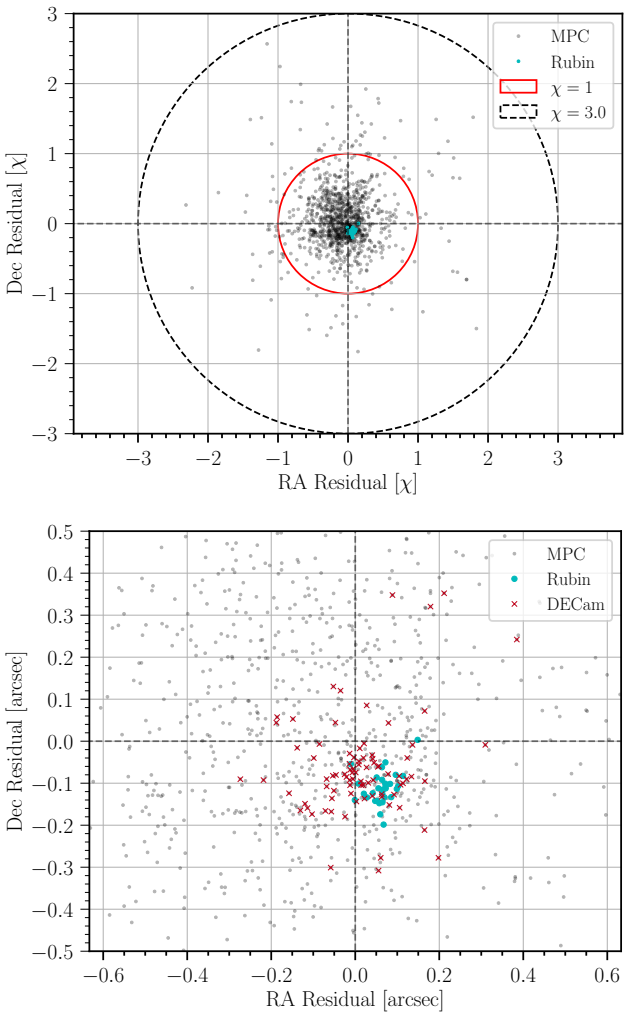


Figure 8. Astrometric residuals of 3I/ATLAS based on data available at the MPC up until 2025-07-15 (MPC Solution 20250715). **Top:** Residuals in Right Ascension corrected for Declination vs Declination plotted in units of the goodness of fit parameter χ. Regions of constant χ are also shown. **Bottom:** Declination-corrected Residuals in Right Ascension vs Declination. In both panels, the Rubin data points are shown as teal circles, data available in the Minor Planet Center are black dots. The bottom panel also includes astrometric data taken with DECam available from the MPC as red markers.

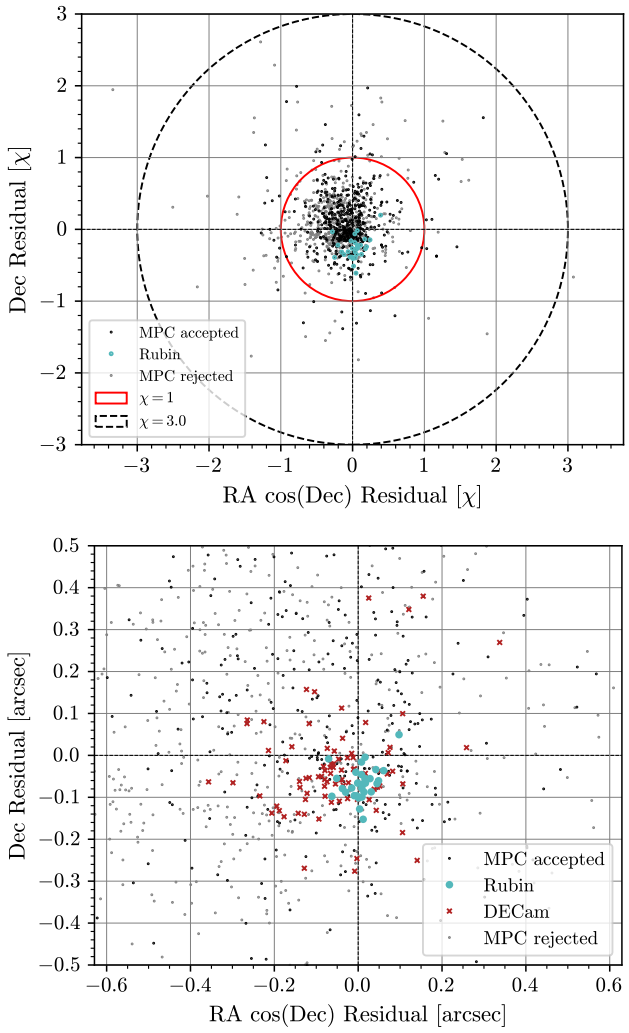


Figure 9. Same as Figure 8 only for Rubin Solution 20250715. Rejected datapoints are shown in grey. **Top:** Residuals in Right Ascension corrected for Declination vs Declination plotted in units of the goodness of fit parameter χ. **Bottom:** Declination-corrected Residuals in Right Ascension vs Declination.

surements presented above. The July 2 data includes 28 r-band observations of 3I/ATLAS within an hour (see Figure 10), which can also be challenging due to the potential for self-subtraction, as the object moves $\lesssim 1$ PSF across two pairs of visits. Another option, which we leave for future work, would be to explore techniques such as scene modeling photometry (*e.g.* Bernardinelli et al. 2023), which can measure the target at multiple images while simultaneously accounting for contamination of background sources.

4.8. *Thermophysical Modeling*

To get a general sense of the rate of temperature change for an airless body at a given distance, we make use of a simple thermophysical model, following Hsieh et al. (2015) and Chandler et al. (2020), whereby a body's heliocentric distance as a function of temperature is given by

$$R(T) = \sqrt{\frac{F_\odot(1-A)}{\chi\left[\epsilon\sigma T^4 + Lf_{\rm D}\dot{m}_{\rm S}(T)\right]}}\ \text{au.}, \qquad (1)$$

Here, $F_\odot = 1360$ W m^{-2} is the solar flux at 1 au, $A = 0.05$ the assumed Bond albedo, $\epsilon = 0.9$ the assumed infrared emissivity of the ice, $T_{\rm eq}$ the equilibrium

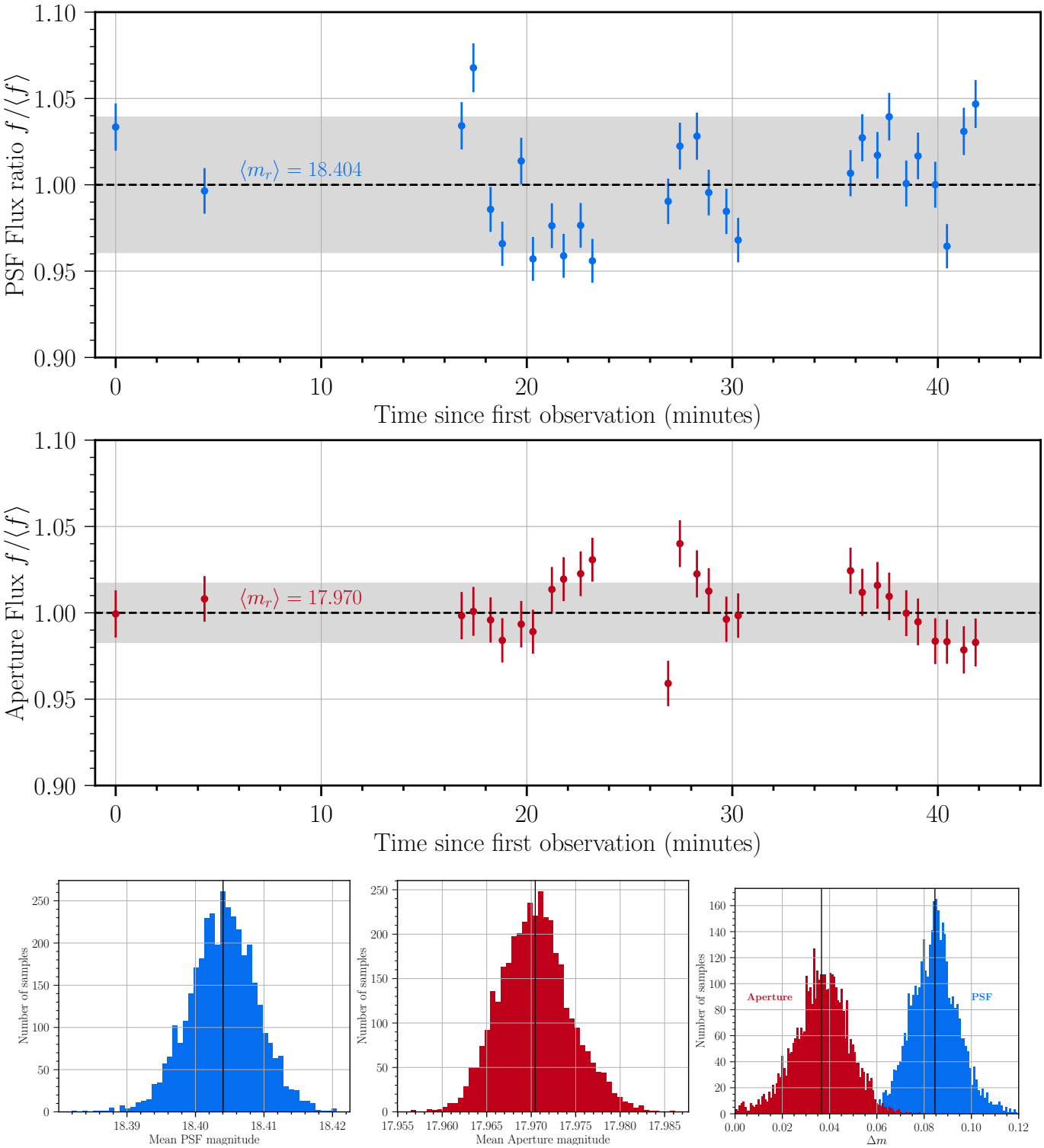


Figure 10. Top: The two horizontal panels show time series PSF and aperture flux measurements $f/\langle f \rangle$ for the 28 viable r band images of 3I/ATLAS taken on July 2nd 2025. The gray shaded area represents the variability expected from the mean light curve amplitude A. **Bottom left:** Probability distribution of the mean PSF magnitude yielded by this procedure, with the vertical line indicating the mean measurement $\langle m_r \rangle = 18.404$ mag, with a standard deviation of 0.005 mag. **Bottom center:** Same as the previous panel, but for the aperture magnitude, where $\langle m_r \rangle = 17.970 \pm 0.004$. **Bottom right:** The probability distribution of the peak-to-peak light curve amplitude (in magnitudes) $\Delta m \equiv 2.5 \log_{10}[(1 + A)/(1 - A)]$ for the aperture (left, $\langle \Delta m \rangle = 0.036 \pm 0.011$) and PSF (right, $\langle \Delta m \rangle = 0.084 \pm 0.010$) flux measurements.

temperature, and $\sigma = 5.670 \times 10^{-8}$ W m^{-2} K^{-4} the Stefan–Boltzmann constant. The parameter χ captures rotational and axial-tilt effects on insolation: $\chi = 1$ corresponds to a "slab" perpetually facing the Sun (resulting in maximum heating), $\chi = \pi$ to a rapid rotator with zero tilt, and $\chi = 4$ is the value we adopt for an isothermal, fast-rotating body in thermodynamic equilibrium.

Figure 11 shows the results of this modeling, along with several other metrics useful for understanding the discovery and future observations of 3I/ATLAS. 3I/ATLAS was at its peak observability (number of hours at night an object is above the horizon) during 2025 June, and it will be less observable from NSF-DOE Vera C. Rubin Observatory during perihelion passage as compared to Northern hemisphere sites.

4.9. *Image Analysis*

4.9.1. *Coma Analysis*

We begin with a radial profile analysis (Figure 12) when 3I/ATLAS was in relative isolation, despite the object transiting a crowded field. We carried out our analyses with 600×600 pixel ($120'' \times 120''$) cutouts (Section 3.1) extracted via the Rubin Science Platform and `astropy`'s `Cutout2D` function, preserving an adequate WCS for the purpose (e.g., matching to Gaia stars). The two 3I/ATLAS-isolated images were from UT 2025 June 21 and UT 2025 July 2.

For each image, we prescribe an aperture sufficient to capture all of the flux of 3I/ATLAS discernible from the background (or noise floor; see below); these were 20 and 30 pixels ($4''$ and $6''$), respectively. We also randomly selected several background stars throughout the field, also in relative isolation, though the field was sufficiently crowded that only a handful of isolated stars were usable. Larger cutouts might have provided additional stars; however, proximate stars are more likely to conform to the same general shape, given that some data were acquired during engineering time. We summed the flux of 3I/ATLAS and the field stars in concentric radial annuli.

In Figure 12 we show the azimuthally averaged radial profile of the reflected light from 3I/ATLAS to show the point spread function compared to that of nearby field stars. The excess of the radial profile compared to that of the nearby stars is indicative of cometary activity. However, the Rubin LSST images are not tracking the motion of 3I/ATLAS and the exposure time of each image is 30 s. Therefore, there will be both trailing loss and smearing of the radial profile with respect to that of the comparison star. To quantify the magnitude of the effect, we first consider the object's apparent sky rates of motion of $\sim 60''$/hr (UT 2025 June 21, Table 2) and $\sim 75''$/hr (UT 2025 July 2). Thus, in each exposure, the object had moved $\sim 0.5''$ (2.5 pixels) and $\sim 0.625''$ (3.125 pixels), respectively. At first glance, this appears to be comparable in magnitude to the offset between the comparison star and the 3I/ATLAS profile (see the region between 0.5 - 7.5 pixels in Figure 12, top panel). However, we note that the smearing of the profile should *only* operate along the direction of motion. Should there be just a trailing starlike nucleus with no coma, we should see at least a few data points representing pixel intensities of 3I/ATLAS that lie along the stellar PSF curve (belonging to pixels lying perpendicular to the motion). We do not see such points, which strongly support the presence of a coma. Therefore, the azimuthal averaging should reduce this effect, and we conclude that there is still evidence for cometary activity.

These images were fully processed by the LSST Science pipelines (Rubin Observatory Science Pipelines Developers 2025) and, consequently, should have already had their background values subtracted. However, (a) commissioning is ongoing, and (b) crowded fields have proven challenging due to the absence of discernible background (i.e., little to no area on the sky without one or more sources in the field). In the case of our two isolated images, the June 21 image underwent background subtraction that resulted in appreciable "negative flux," and the July 2 image still had some background flux measurable in our aperture.

To remedy the discrepant background levels, we fit a polynomial function to each set of data points and derive a limit determined by the inflection point, at which the curve reaches its floor. For the UT 2025 June 21 data, 3I/ATLAS has an apparent radial extent of 11.75 pixels ($2.35''$), or $\sim 6,520$ km. On UT 2025 July 2, 3I/ATLAS had a radial extent of 18.64 pixels ($3.73''$), or $\sim 9,384$ km. In both cases, these should be considered very conservative lower limits as the object appeared nearly head-on, so the tail could have extended far along the z-axis (as projected on the sky).

We show contour plots of science images of 3I/ATLAS from UT 2025 June 21 at 08:11:33 UTC and UT 2025 July 2 at 03:33:02 UTC in which the object is largely isolated from background sources in Figure 7. On June 21, the target appeared somewhat extended in the East-West direction, although this was also the direction of its apparent non-sidereal motion. Therefore, this morphology may have been due to the trailing of the object in these sidereally tracked images. On July 2, the target appeared to have a notably extended and asymmetric coma, with a PA at roughly 290° East of North, very nearly opposite the direction of the PA of the projected

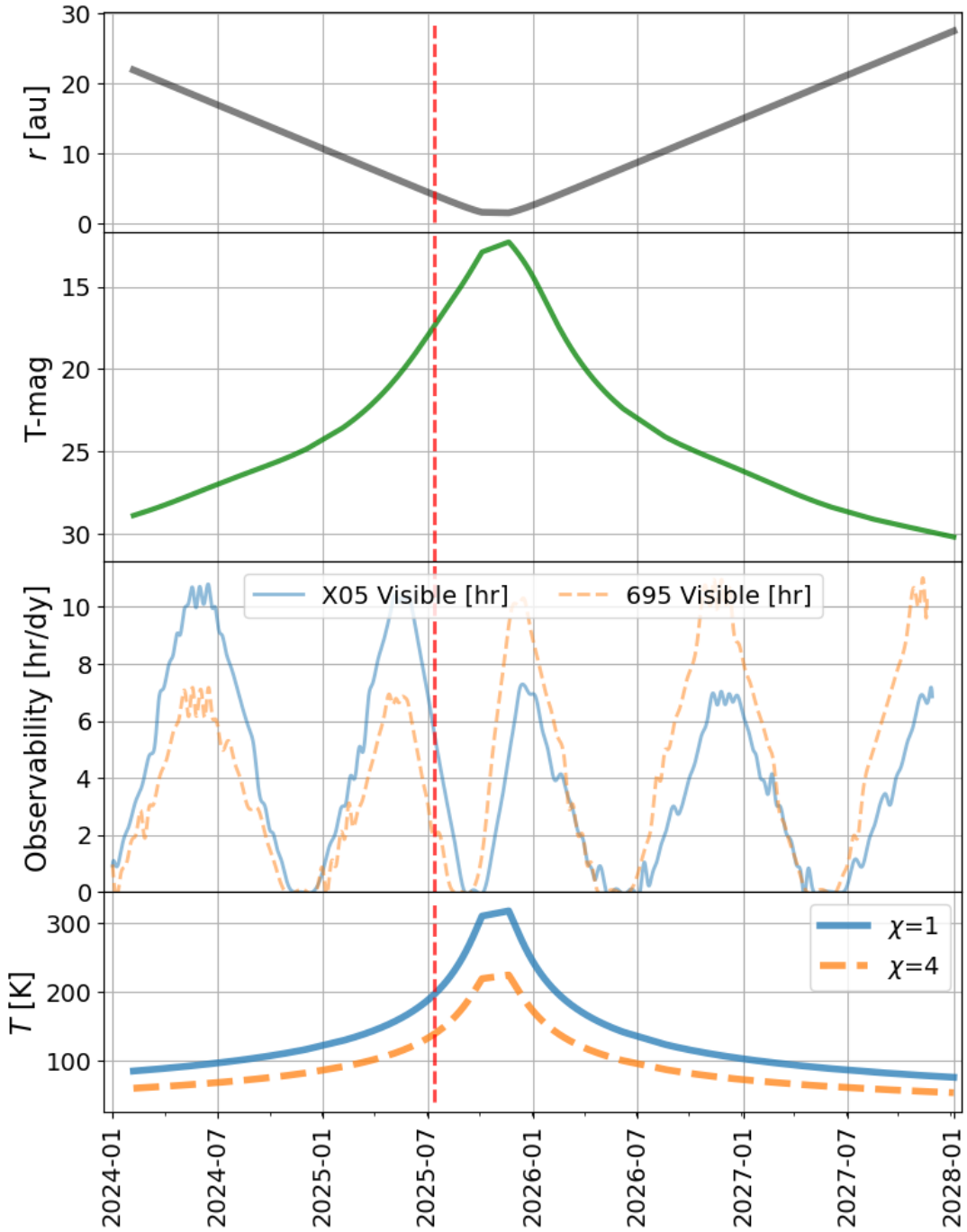


Figure 11. 3I/ATLAS metrics plotted versus time from UT 2024 January 1 to UT 2028 January 1. The vertical dashed red line indicates UT 2025 July 12; this is the date elements were retrieved from JPL Horizons (Giorgini et al. 1996). The r [au] panel indicates the heliocentric distance of 3I/ATLAS. The T-mag panel indicates the JPL Horizons-computed total magnitude of 3I/ATLAS; T-mag should be considered a *very* rough estimate, and is included here to provide a general sense of expected brightness behavior rather than a quantitative or predictive tool. The Observability [hr/dy] panel describes the number of nighttime hours 3I/ATLAS spends above the horizon for a given UT night at the specified observatory. Kitt Peak National Observatory (695) and Rubin Observatory (X05) are chosen as representative Northern and Southern hemisphere sites, respectively. The T [K] panel provides a simple temperature estimate for a representative airless body, where $\chi = 4$ represents the isothermal case (e.g., fast-rotator) and $\chi = 1$ corresponds to the "flat slab" scenario, which is the thermophysical extreme. These lines are to provide context only and do not represent actual temperatures on 3I/ATLAS.

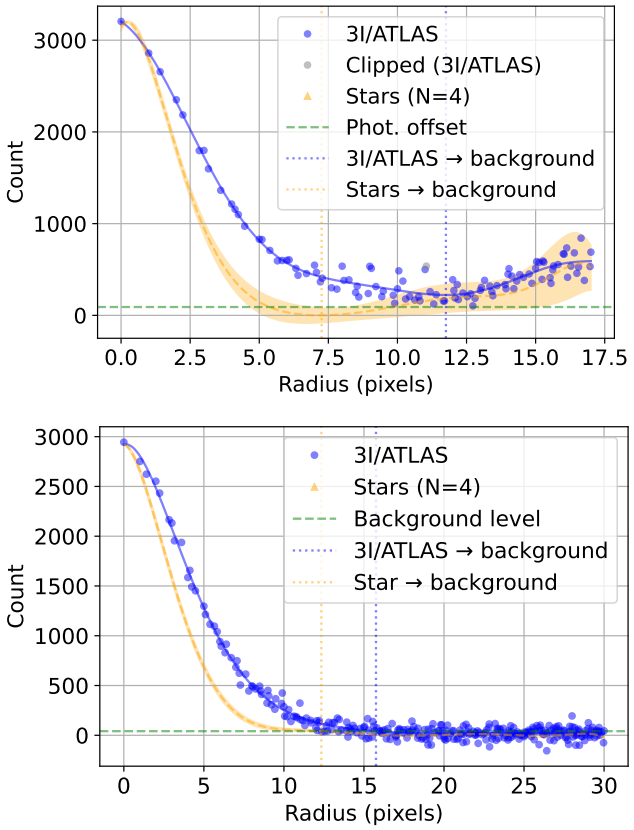


Figure 12. Radial profile measurements of 3I/ATLAS (blue circles) and a set of four vetted comparison stars (yellow shaded region), along with polynomial fits (solid blue line and dashed yellow line, respectively). Data points beyond 3σ from the polynomial fit were clipped (grey markers, when present), and the function was re-fit. The signal floor is indicated by a horizontal green dashed line. Vertical dashed lines indicate the radial extent of 3I/ATLAS (blue) and the mean of the comparison stars fit (yellow). **Top:** 2025-06-21. Coma extent at 11.75 px: ∼6,520 km. $r_H = 4.834$ au. The signal floor is below zero flux, so a photometric offset has been applied to the fit. **Bottom:** 2025-07-02. Coma extent at 18.64 px: ∼9,380 km. $r_H = 4.476$ au. Residual background signal was measurable, so additional background subtraction was incorporated into the measurements.

anti-solar vector. In other words, rather than pointing away from the Sun as is normally expected, 3I/ATLAS's tail appeared to be pointing toward the Sun. We discuss this unexpected behavior below in Section 4.9.3.

In order to characterize the amount of coma present on these different dates, following Luu & Jewitt (1992) and Hsieh & Jewitt (2005), we performed an analysis in which we compare one-dimensional surface brightness profiles of the comet, as measured perpendicularly to the direction of apparent non-sidereal motion, to those of template field stars with varying amounts of synthetically added spherically symmetric and steady-state coma following a r^{-1} radial surface brightness profile, where r is the angular distance from the photocenter as projected on the sky. In this modeling analysis, coma levels were parameterized by $\eta = C_c/C_n$, where C_c and C_n were the total scattering cross-sections from the coma and nucleus (assuming that both have the same effective albedos), respectively, where we used a reference photometry aperture of $r_{\rm phot} = 5\farcs5$ for measuring these fluxes.

For measuring one-dimensional surface brightness profiles, we rotated images of 3I/ATLAS and a selected well-isolated field star in each image to align the direction of motion horizontally in the image frame, where in this case, the non-sidereal motion of 3I/ATLAS was very nearly exactly West to East on June 21 and July 2, and so the orientations of the rotated images are virtually identical to those of the images in Figure 2 and contour plots in Figure 7. We then averaged pixel values over horizontal rows over the entire widths of the object and reference stars, and subtract sky background sampled from nearby areas of blank sky. Object and model profiles were then normalized to unity at their peaks and plotted together (Figure 13) to search for the closest matching model profile to each object profile.

Adding synthetic coma using the method described above has less effect on surface brightness profile cores then it does on profile wings, but of course the profiles are more impacted by noise farther from a particular source's photocenter. As such, we focus on examining the deviation of the comet profile close enough to the center where the signal is relatively strong, profiles vary relatively smoothly, and the r^{-1} coma profile assumption used in our model is more likely to be true, but far enough away that the model profiles using different coma levels show visible separation from one another. For profile plots on both dates, this range of interest is approximately $0\farcs4$ to $0\farcs7$ from the photocenter.

We find that coma is clearly present for 3I/ATLAS in the June 21 08:11:33 image (Figure 13a) at a level of $\eta \sim 2.0 \pm 0.5$, where the uncertainty is estimated based on visually identifying the synthetic coma profiles that bound the comet profile. Meanwhile, we find an approximate coma level of $\eta \sim 2.5 \pm 0.5$ for the July 2 03:33:02 image (Figure 13b), indicating that the coma may have increased slightly over the 11 days between the two observations (although we also note that the coma level estimates are also consistent within their estimated uncertainties between the two dates). That said, we also see a larger extension of the surface brightness profile on the North side of the comet, which is corroborated by the visible asymmetry of the comet in its contour plot from that date (Figure 7b). As such, we consider

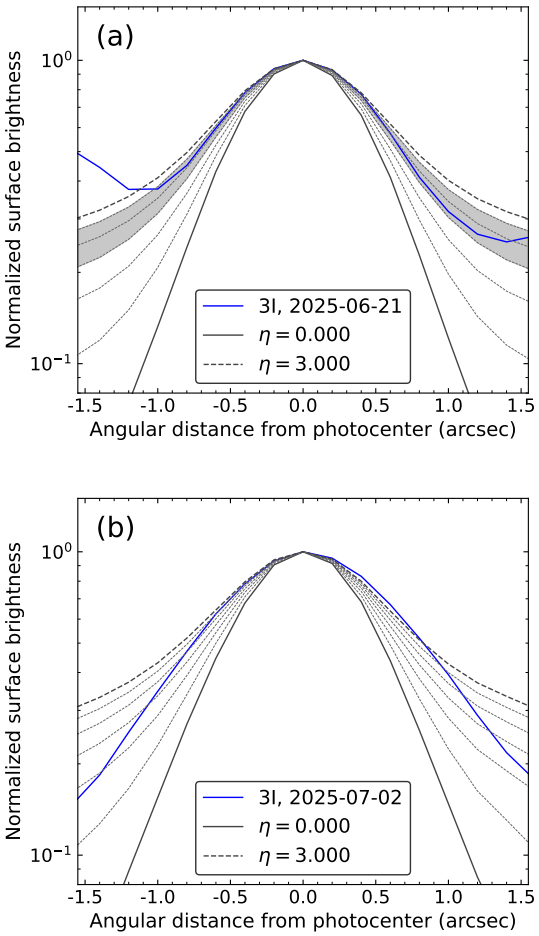


Figure 13. One-dimensional surface brightness profiles (measured perpendicular to the direction of apparent non-sidereal motion) of 3I/ATLAS (solid blue lines) and seeing-convolved model nuclei with linearly spaced coma levels (i.e., $\eta_i = 0.5(i-1)$) ranging from $\eta = 0$ (solid black lines) to $\eta = 3$ (dashed black line, with profiles corresponding to intermediate η values shown as dotted black lines) for data from (a) UT 2025 June 21, and (b) UT 2025 July 2. Estimated uncertainty regions, i.e., the regions bound by the model profiles adjacent to the best-matching model profile in each panel, are shaded in gray.

the estimated increase in coma level of $\Delta\eta \sim 0.5 \pm 0.5$ between June 21 and July 2 to be a lower limit.

4.9.2. *Nucleus Analysis*

The well-isolated July 2 03:33:02 detection of 3I/ATLAS (see Figure 7b) had a measured i-band aperture magnitude of $m_i = 17.633 \pm 0.006$ as measured in a circular aperture with a radius of 3.″4 (17 pixels, or 8,600 km at the geocentric distance of the comet), where we note that this value differs from the PSF magnitude reported for that detection in Table 1 given that aperture photometry does not effectively exclude the dust coma as is the case with PSF-fit-derived photometry.

On July 2, 3I/ATLAS had heliocentric distance of $r_h = 4.48$ au, a geocentric distance of $\Delta = 3.47$ au, and a solar phase angle of $\alpha = 2.3°$. In order to estimate the object's nucleus size, we first compute a reduced magnitude, $m(1, 1, \alpha)$, i.e., normalizing the measured apparent aperture magnitude to $r_h = \Delta = 1$ au using

$$m_i(1, 1, \alpha) = m_i(r_h, \Delta, \alpha) - 5\log(r_h\Delta) \quad (2)$$

Given that the nucleus and dust are expected to have different phase darkening behavior, we then partition this reduced magnitude into its nucleus and dust components using the coma level estimated from our surface brightness profile analysis for July 2 of $\eta = 2.5 \pm 0.5$ (Section 4.9.1), where the nucleus is assumed to account for $1/(3.5\pm0.5)$ of the observed flux and the dust coma is assumed to account for $2.5/(3.5\pm0.5)$ of the observed flux, obtaining a nuclear magnitude of $m_{i,n}(1, 1, \alpha) = 13.04 \pm 0.16$ and a dust coma magnitude of $m_{i,d}(1, 1, \alpha) = 12.04 \pm 0.16$.

Adopting Jupiter-family comet (JFC) nuclei as a potentially reasonable proxy for the nucleus of 3I/ATLAS, we use the median linear phase coefficient and standard deviation of $\beta = 0.046 \pm 0.017$ mag deg^{-1} found from measurements of a large sample of JFC nuclei by Kokotanekova et al. (2017). Correcting for $\alpha = 2.3°$ therefore results in an absolute magnitude of $H_{i,n} = m_{i,n}(1, 1, 0) = 12.93 \pm 0.16$.

Meanwhile, we use the Schleicher-Marcus phase function[7] (sometimes also referred to as the Halley-Marcus phase function; Schleicher & Bair 2011; Schleicher et al. 1998; Marcus 2007) for determining the phase darkening correction of the dust component of this observation, finding that the expected observed flux at $\alpha = 2.3°$ is 0.91 of the expected observed flux at $\alpha = 0°$. We therefore obtain $H_{i,d} = m_{i,d}(1, 1, 0) = 11.94 \pm 0.16$.

Lastly, we combine the distance- and phase-corrected magnitudes of 3I/ATLAS's nucleus and dust components using

$$m_{i,\mathrm{tot}} = -2.5\log\left(10^{-0.4m_{i,n}(1,1,0)} + 10^{-0.4m_{i,d}(1,1,0)}\right) \quad (3)$$

obtaining a total absolute magnitude of $m_{i,\mathrm{tot}}(1, 1, 0) = 11.57 \pm 0.12$. We note that the above calculations assume that the dust coma is optically thin, and utilize the `uncertainties` python package for the calculation and propagation of uncertainties[8].

[7] https://asteroid.lowell.edu/comet/dustphase.html
[8] https://pythonhosted.org/uncertainties/

In order to estimate 3I/ATLAS's nucleus size from the absolute magnitude found above, we first convert the i-band absolute magnitude to r-band using the $(r-i)_{\rm LSST}$ color as computed in Appendix B, obtaining $H_{r,n} = H_{i,n} + 0.299 = 13.23 \pm 0.16$. We then compute an equivalent V-band absolute magnitude, $H_{V,n}$, using

$$H_{V,n} = H_{r,n} + 0.73(V-R) - 0.088 \quad (4)$$

from Jordi et al. (2006), where we use $V-R = 0.716$, as computed using 3I/ATLAS's reported spectral slope of $S' = 18\%/100$ nm. We obtain $H_{V,n} = (13.66 \pm 0.16)$ mag, or over 1 mag fainter than the H_V value ($H_V > 12.4$) estimated by Seligman et al. (2025) based on ZTF precovery data. Finally, we can estimate the effective nucleus radius using

$$r_n = \left(\frac{2.24 \times 10^{22}}{p_V} \times 10^{0.4(m_{\odot,V} - H_V)} \right)^{1/2} \quad (5)$$

where we use $m_{\odot,V} = -26.71 \pm 0.03$ for the apparent V-band magnitude of the Sun (Hardorp 1980) and assume a V-band geometric albedo of $p_V = 0.05$ (typical of reddened comet nuclei; Knight et al. 2024), finding $r_n = (5.6 \pm 0.7)$ km, about half of the previous nucleus size upper limit estimate by Seligman et al. (2025). Given that this nucleus size is based on a coma-to-nucleus ratio that we expect to be underestimated (see Section 4.9.1), we regard this result as an upper limit to 3I/ATLAS's true nucleus size. We further note that it is based on assumptions of spherically symmetric, steady-state coma, which we know is not the case (discussed below in Section 4.9.3), as well as identical geometric albedos for coma grains and the nucleus, for which we have no direct constraints. As such, while we consider this result to be an advance over previous work, we note that further work to directly observe 3I/ATLAS's nucleus with high-resolution imaging by space telescopes like the *Hubble Space Telescope* and *JWST* will be extremely useful for confirming or refining its size.

Adopting our nucleus size upper limit as the true nucleus size for now, we can get a sense of the potential mass loss rate, $\dot{M}$, from η using

$$\dot{M} = \frac{(1.1 \times 10^{-3}) \pi \rho_d \bar{a} \eta r_{\rm obj}^2}{p r_h^{0.5} \Delta} \quad (6)$$

(Luu & Jewitt 1992), where ρ_d is the average bulk dust grain density, $\bar{a}$ is the weighted mean grain radius, $r_{\rm obj}$ is the object's effective radius, p is the angular photometry radius in arcseconds, and r_h and Δ are the heliocentric and geocentric distances in au. In addition to the uncertainty on our nucleus size estimate, there are currently no useful empirical constraints on ρ_d and $\bar{a}$. While ρ_d may vary by a factor of a few among different materials, $\bar{a}$ dominates the uncertainty as it can vary by several orders of magnitude (e.g., from μm to mm scales or larger). For illustration, for arbitrary assumptions of $\rho = 1000$ kg m^{-3} and $\bar{a} = 1$ μm, we obtain $\dot{M} \sim 10$ kg s^{-1}, but $\bar{a} = 10$ μm would result in $\dot{M} \sim 100$ kg s^{-1}. Constraints on particle sizes (which may change with heliocentric distance), e.g., via detailed dust modeling, will be critical for deriving more realistic mass loss rates for 3I/ATLAS in the coming months as it becomes more active.

For reference, we also calculate the $A(\alpha = 0^\circ) f\rho$ parameter (hereafter, $Af\rho$; A'Hearn et al. 1984), which is frequently used to parameterize dust production rates, and is given by

$$A(\alpha = 0^\circ) f\rho = \frac{(2 r_h \Delta)^2}{\rho_{ap}} 10^{0.4[m_\odot - m_d(r_h, \Delta, 0)]} \quad (7)$$

where r_h is in au, Δ is in cm, ρ_{ap} is the physical radius in cm of the photometry aperture used to measure the magnitude of the comet at the distance of the comet, $m_\odot$ is the apparent magnitude of the Sun at $\Delta = 1$ au in the same filter used to observe the comet, and $m_d(r_h, \Delta, 0)$ is the phase-angle-corrected (to $\alpha = 0^\circ$) apparent magnitude of the dust with the flux contribution of the nucleus subtracted from the measured total magnitude. For this calculation, the nucleus contribution to the flux is calculated assuming a linear phase function and median linear phase coefficient from a sample of JFC nuclei from Kokotanekova et al. (2017), and the nucleus-subtracted magnitude of the dust is corrected to $\alpha = 0^\circ$ using the Schleicher-Marcus phase function as discussed above. Using parameter values specified above, we compute $Af\rho = (315 \pm 15)$ cm in i-band, which is slightly larger than the i'-band $Af\rho = (288 \pm 5)$ cm value (using a photometry aperture with a radius of 4″, or about 10,000 km at the distance of the comet) reported by Bolin et al. (2025).

4.9.3. *Tail Analysis*

As noted by several observers (Jewitt & Luu 2025; Alarcon et al. 2025; Seligman et al. 2025; Opitom et al. 2025; Bolin et al. 2025), 3I/ATLAS is observed to exhibit a short sunward-pointing tail in imaging data obtained since its discovery. While such a morphology is certainly unusual—given that dust tails are typically directed antisolar due to radiation pressure acting on dust grains—it is not without precedent among distant active bodies. Notably, Farnham et al. (2021) reported a similar sunward enhancement in comet C/2014 UN$_{271}$ (Bernardinelli–Bernstein), which they interpreted as the result of the slow ejection of relatively large dust particles predominantly from the sunlit hemisphere. Simple

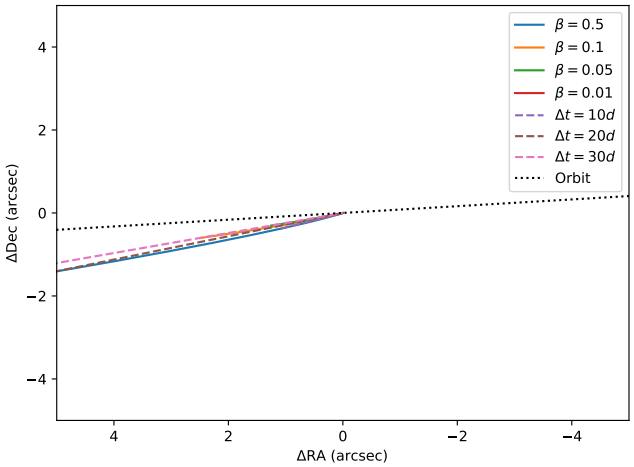


Figure 14. Synchrone-syndyne grid for 3I/ATLAS on UT 2025 July 2 for isotropic dust emission. The position of the object is at the center of the plot (at ΔRA = ΔDec = 0 arcsec), where (essentially overlapping) solid colored lines correspond to syndynes, along which particles of specified sizes should be found (where particle sizes are parameterized by β; particle radii, a, in μm, are approximately given by $a = \beta^{-1}$), dashed colored lines correspond to synchrones, along which particles ejected at specified times should be found (synchrones shown for 10, 20, and 30 days prior to the current epoch), and the dotted black line shows the projection of the orbital plane on the sky.

Finson-Probstein-style dust modeling (Finson & Probstein 1968a,b) carried out using the `SynGenerator` class[9] in `sbpy` (Mommert et al. 2019) to generate and plot syndynes and synchrones for 3I/ATLAS shows that, for isotropic dust emission (which is typically assumed), any dust tail should have a PA of ∼100° East of North (Figure 14). 3I/ATLAS's approximately sunward tail (PA ∼ 290°) strongly implies the presence of anisotropic dust emission (e.g., Hsieh et al. 2011; Farnham et al. 2021; Hsieh et al. 2025), specifically with an average direction in the orbit plane (which is close to the ecliptic plane), given the sunward tail's approximate orientation along the direction of heliocentric motion. Although the sunward feature observed in 3I/ATLAS is broadly consistent with anisotropic dust emission, such a morphology can also arise from gas jets, as observed in comets like C/1996 B2 (Hyakutake), where strong sunward CN and C_2 emissions were detected in narrowband images (Rodionov et al. 1998). However, optical spectroscopy of 3I/ATLAS on 2025 July 3 did not detect any gas (Opitom et al. 2025).

[9] https://sbpy.readthedocs.io/en/latest/sbpy/dynamics.html#dust-syndynes-and-synchrones

We note that the implication of anistropic dust emission close to the ecliptic plane raises the possibility of a nearly in-plane rotation pole, since the time-averaged direction of a non-equatorial jet is equivalent to the direction of the nearest rotation pole (e.g., see Hsieh et al. 2011). Such geometry could, in principle, allow pole-on viewing orientations with respect to the Earth (e.g., Buie et al. 2018), which would in turn be consistent with only minor light curve variations being reported for 3I/ATLAS thus far in this work (Section 4.7) and by others (e.g., Seligman et al. 2025). That said, the small light curve ranges observed thus far could also be partially or even entirely due to the damping effects of a steady-state coma on the observable light curve variations of an underlying rotating nucleus (e.g., Hsieh et al. 2011). Finally, it is important to keep in mind that the detailed geometry of dust emission depends critically on nucleus shape. Small cometary nuclei are frequently irregular or contact binary objects, often characterized by deep concavities capable of producing focused sunward jets. For example, in comet 67P/Churyumov–Gerasimenko, such topography-induced sunward jets were well documented by Rosetta (e.g., Shi et al. 2018). Without knowledge of 3I/ATLAS's nucleus shape, no firm conclusion on the physical cause of its coma morphology can be drawn.

4.10. *Discoverability of of 3I/ATLAS and Prospects for Future Observations in the SV Survey*

The SV survey is intended to behave much like the operations LSST survey strategy. In the SV survey, observations are typically obtained in pairs of exposures separated by approximately 30 minutes, as is the case in the operations survey. However, the SV survey is attempting to gather on the order of 1-2 years worth of operations LSST images (about 150 exposures) within 2-3 months of commissioning time. To achieve this goal, the pointings within the main SV footprint are generally covered every night, instead of every few nights as in the operations survey. In addition, the primary SV survey footprint is much smaller than the full LSST footprint. The primary SV survey covers a region along the ecliptic plane, stretching across a wide variety of galactic latitudes including the Galactic plane itself. This provides tests of pipelines in both crowded and less dense fields, as well as the maximum opportunity to commission the Solar System linking pipelines.

The SV survey is both similar and dissimilar to the nominal upcoming LSST (baseline_v4.0; Yoachim 2025; Jones et al. 2025) during comparable periods (i.e. between May and August, centered on 3I's discovery). The SV footprint is much more compact, predominantly following the ecliptic plane, with the exception of the Deep

Drilling Fields (DDFs). While the exact frequency and quality of images may differ both SV and LSST provide relatively uniform coverage over the regions of sky included.

An early simulation of the entire SV survey period was released alongside Claver et al. (2025). This simulation was created by the Feature Based Scheduler (Yoachim et al. 2025a; Naghib et al. 2019), much as the baseline operations survey is simulated. As the SV survey progresses, these simulations are updated by including information about exposures acquired to-date, obtained from the LSST Consolidated Database (Lim 2025), alongside attempts to improve the fidelity of the observatory model. The already-acquired exposure information is fed into the scheduler, then the simulation is continued for the remainder of the SV period. One such simulation was created containing the pointing history of the SV survey as of the start of observing on UT 2025 July 14 ('sv_20250714'), which was used to evaluate both the likelihood of acquiring 3I/ATLAS in already acquired visits and the possibility of future detections.

4.10.1. *Discoverability of 3I/ATLAS*

We used the ISO survey simulation framework outlined in Dorsey et al. (2025) to simulate the probabilistic observability of 3I/ATLAS in the LSST SV survey. We simulate 10,000 clones, each sampled from the covariance matrix of 3I/ATLAS's orbit (retrieved from JPL Horizons on 2025 July 15), and assess which SV pointings would have observed an object of similar absolute magnitude and color (Table A1), applying the LSST Solar System Processing (SSP) criteria for moving object discovery. For this analysis, we use the preliminary value of $H_r \sim 12.5$ for 3I/ATLAS that was available at the time of this analysis. As anticipated, all clones were detected and subsequently discovered within the SV survey: the apparent magnitude of 3I/ATLAS ($m_r \sim 18$ mag) is 5 magnitudes brighter than the median limiting magnitude of LSST in r-band (S1). For 95% of the clones, the first successful observation occurred on UT 2025 June 21 (MJD 60847.155) and discovery occurred 13 days later, on UT 2025 July 4 (MJD 60860.998). None of the clones were discovered earlier than 2025 July 2 (the date of discovery by ATLAS). This simulation demonstrates that had the SV begun two weeks earlier and pipelines run as in LSST, LSST may have indeed discovered 3I/ATLAS prior to ATLAS.

4.10.2. *Future Prospects in the SV Survey*

To assess the detectability of 3I/ATLAS over the remainder of the SV survey, we employed the survey simulator `Sorcha` (Merritt et al. 2025; Holman et al. 2025), incorporating the actual pointing history and environmental conditions of the observatory to date and the ideal best-case SV cadence simulation. A synthetic 3I/ATLAS using H_r=12.5 was generated from its best-fit orbital elements at the time of writing $\{q, e, i, \omega, \Omega, T_P\} = \{1.357$ au, 6.147, 175.113°, 322.165°, 127.999°, JD 2459860.3$\}$ assuming colors estimated in Appendix B (see Table A1) and a phase curve G parameter of 0.15. Given the uncertainty in how sublimation and dust production will vary with changing heliocentric distances, we make no attempt to model the flux enhancement from reflected sunlight by 3I/ATLAS's coma/tail and model 3I/ATLAS's apparent brightness as an airless non-active body. Our results therefore are a lower limit on detectability, but as the apparent magnitude of 3I/ATLAS in the Rubin images is well above the 5-σ source detection limit of the SV survey, the impact from ignoring cometary activity is negligible on our predictions.

We first validated the simulator by reproducing all SV observation Visit IDs obtained to date, recorded in Table 1 and then extended our simulation forward to the nominal SV conclusion (UT 2025 September 22). The cumulative sky-map of predicted 3I/ATLAS detections is presented in Figure 15 (an animation of the figure is available in the online version of the paper). Our predictions indicate that, beyond the last recorded detection, 3I/ATLAS should be recovered in as many as approximately 100 additional SV exposures, including a ToO sequence on 2025 July 12. The expected distribution of visits per filter is very roughly 30 in g, 20 in each of r and i, and 10 for u, z, and y. The object's mean apparent magnitude across the $griz$ bands remains $m \approx 18.3$, in line with estimates from Figure 10, assuming no cometary activity brightening. The simulation predicts that 3I/ATLAS will remain brighter than the survey's nominal detection threshold until 3I/ATLAS moves out of the SV survey footprint on UT 2025 August 22, approximately one month prior to the SV survey's scheduled end.

4.11. *Implications for the ISO Luminosity Function*

The estimated nuclear size of 3I/ATLAS ($H_{V,n} = 13.7 \pm 0.2$ mag or $H_{r,n} = 13.2 \pm 0.2$ mag) from LSST photometry has important implications for the size-frequency distribution of the galactic population of ISOs. The detections of 1I/'Oumuamua and 2I/Borisov as significantly smaller interstellar objects ($r \sim 100$ m and $r \sim 400$ m respectively) implied an intrinsically steep size-frequency distribution ($q_s \sim 3$–4; Jewitt et al. 2020), which would agree with historical non-detections of ISOs in Solar System surveys. This constraint is con-

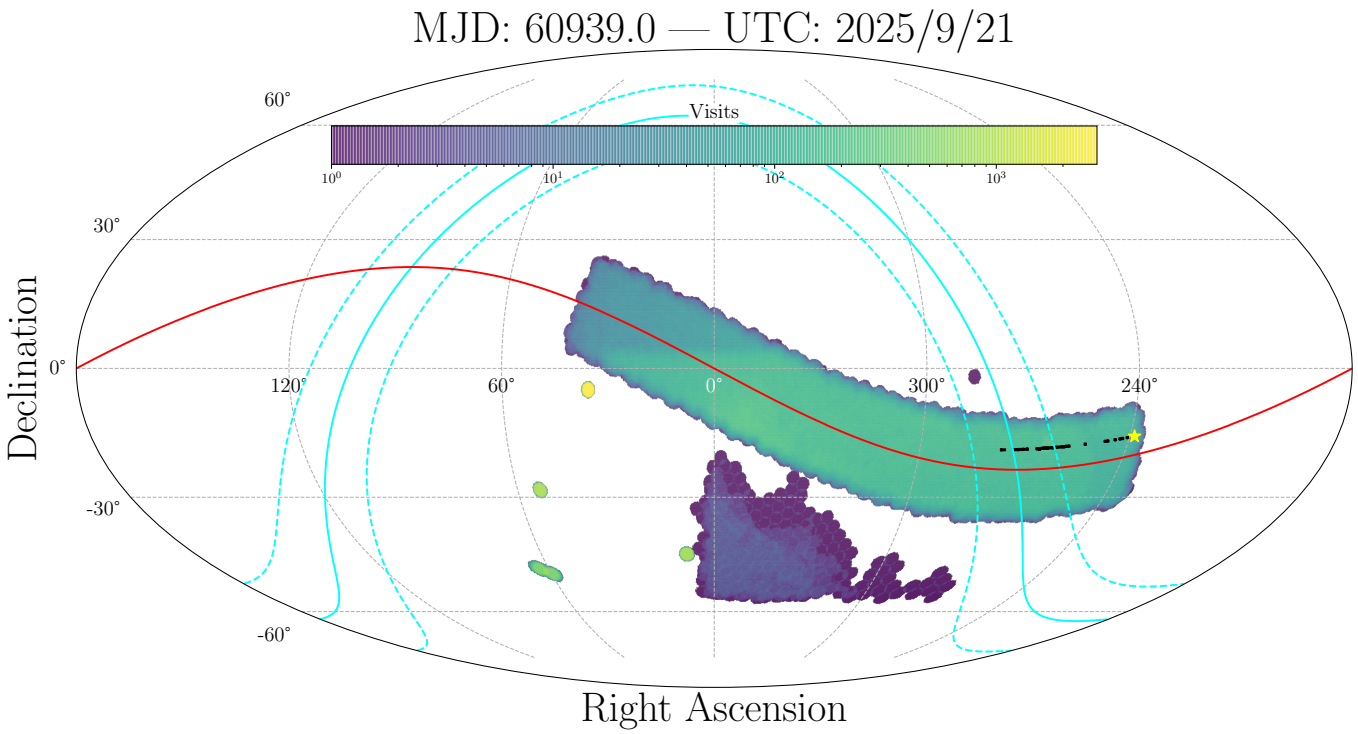


Figure 15. Sky-map of the final SV observations distribution of 3I/ATLAS. The SV here is simulated from recorded pointings already enacted and nominal operations thereafter. The black points represent individual observations of 3I/ATLAS, with the yellow star highlighting its final observation in the SV on UT 2025 August 22. The red solid line marks the ecliptic plane, and the solid and dashed blue lines mark the galactic plane $\pm 10^\circ$. (An animation of this figure is available showing the expected progression of 3I/ATLAS detections during the nominal Rubin Observatory SV survey.)

sistent with other small body populations within the Solar System, from the "primordial" (e.g., large hot classical Kuiper Belt objects (KBOs); Petit et al. 2023) to the more collisionally evolved (e.g., main-belt asteroids; Alvarez-Candal & Licandro 2006). However, as 3I/ATLAS has an absolute magnitude much lower than either of its predecessors, its discovery strongly disfavors a steep slope, instead favoring slopes $q_s \lesssim 3$ (Dorsey et al. 2025). This apparent contradiction can be resolved by instead considering that the intrinsic ISO Size-Frequency Distribution (SFD), which is cumulative across all donor planetary systems, is likely not parameterized by a single slope power law. It is rather a piecewise function of several such power laws with "breaks" — forming a "wavy" SFD — similar to that demonstrated in our own Solar System (Bottke et al. 2023). If the latter, 3I/ATLAS provides the first evidence to begin constraining the shape of the ISOs population SFD.

5. SUMMARY AND DISCUSSION

We report the analysis of the third interstellar object, 3I/ATLAS, obtained from images taken during commissioning of the Rubin Observatory, from UT 2025 June 20 to UT 2025 July 7, coinciding with the start of the Observatory's SV survey. At the time of these observations, although only a portion of the data analysis and management system was deployed and verified, we obtained science-quality photometric and astrometric measurements via a combination of deploying Rubin data management software and bespoke and/or manual techniques. Even in a state of early commissioning, our analysis shows that Rubin Observatory is already capable of delivering high-grade science photometric and astrometric observations of Solar System small bodies.

Below, we summarize our key findings:

- Rubin images clearly show the interstellar object 3I/ATLAS with a dust coma, indicative of activity. These observations provide the earliest high-resolution evidence of detected cometary activity.
- Rubin multi-filter photometry is consistent with previous observations in the literature, with significantly smaller error bars. There are not sufficient same-night multi-filter observations to examine surface/coma color or color evolution, but sufficient to exclude photometric variability on short timescales.

- The coma's radius appeared to increase slightly over the 11 days from $\sim$ 6,520 km (UT 2025 June 21) to $\sim$9,380 km (UT 2025 July 02) as measured from azimuthally averaged radial profiles. We estimate an increase in coma level of $\Delta\eta \sim 0.5$ between 2025 June 21 June and 2025 July 2, which we assume to be a lower limit for several reasons, including that 3I/ATLAS was observed nearly head-on (very low phase angle) and the tail could have extended far along the z-axis, as projected on the sky.

- We obtain a V-band absolute magnitude of $H_V = (13.7 \pm 0.2)$ mag and equivalent effective radius of $\sim (5.6 \pm 0.7)$ km for the nucleus, assuming a spherically symmetric steady-state coma. Due to this simplifying assumption, we consider the latter result to be an upper limit to the true nucleus size. We estimate a mass loss rate ranging from 10 to 100 kg/s, depending on the grain sizes assumed to dominate, and we compute $Af\rho = (315 \pm 15)$ cm for data obtained on UT 2025 July 2.

- We detect no short-term photometric variability. A sequence of measurements taken on UT 2025 July 2 constrains the apparent brightness variations of 3I/ATLAS to less than 0.1 mag on timescales of less than an hour.

- If the Rubin SSP pipelines had been processing the commissioning data in real time, our modeling shows that there were sufficient SV observations to identify 3I/ATLAS as a moving object.

- If the nominal SV survey strategy continues as planned, 3I/ATLAS should be observed in ten or more observations in each filter through mid August 2025. Future SV observations will likely be able to monitor the coma color as 3I/ATLAS moves towards perihelion.

- Analysis of the derived astrometry suggest that for bright high-SNR and extended active small bodies, the combination of Rubin's large aperture and LSSTCam's pixel scale are less impacted by asymmetrical coma provided precise positions for deriving accurate orbital parameters.

The spatial number density of ISOs remains poorly constrained, with forthcoming surveys expected to significantly advance our understanding of this population. Given its large étendue, the LSST is expected to play a major role in this endeavor with Dorsey et al. (2025) estimating that it will identify $\sim$5-50 interstellar objects over its nominal 10 year lifetime. The discovery of a third macroscopic body originating from outside of our Solar System by ATLAS lends further credence to this view, providing tantalizing evidence that a large reservoir of similar bodies may exist within reach of the discovery capabilities of Rubin (Cook et al. 2016; Engelhardt et al. 2017; Marčeta & Seligman 2023; Dorsey et al. 2025). If this is correct, we are about to enter a decade of large-scale discoveries, follow-up, and characterization of this exciting new population.

ACKNOWLEDGMENTS

This material is based upon work supported in part by the National Science Foundation through Cooperative Agreements AST-1258333 and AST-2241526 and Cooperative Support Agreements AST-1202910 and 2211468 managed by the Association of Universities for Research in Astronomy (AURA), and the Department of Energy under Contract No. DE-AC02-76SF00515 with the SLAC National Accelerator Laboratory managed by Stanford University. Additional Rubin Observatory funding comes from private donations, grants to universities, and in-kind support from LSST-DA Institutional Members.

COC thanks Arthur and Jeanie Chandler for their ongoing support.

COC, WB, MW, MT, and DO acknowledge support through Schmidt Sciences LLC. M.J., P.H.B, C.O.C, and D.S. acknowledge support from the DiRAC Institute in the Department of Astronomy at the University of Washington. The DiRAC Institute is supported through generous gifts from the Charles and Lisa Simonyi Fund for Arts and Sciences, and the Washington Research Foundation. M.J. acknowledges the tremendous patience and unwavering support from Dea, Lyra, and Mila throughout the two-decade journey that led to this moment.

M.J.H. gratefully acknowledges support from the NSF (grant No. AST2206194), the NASA YORPD Program (grant No. 80NSSC22K0239), and the Smithsonian Scholarly Studies Program (2022, 2023).

S.E. acknowledges support by the National Science Foundation under Grant AST-2307570. R.M. acknowledges funding from a NASA Space Technology Graduate Research Opportunities (NSTGRO) award, NASA contract No. 80NSSC22K1173.

`sbpy` is supported by NASA Planetary Data Archiving, Restoration, and Tools (PDART) Grant Numbers 80NSSC18K0987 and 80NSSC22K0143.

Gy.M.Sz acknowledges support from SNN-147362 of the National Research, Development and Innovation Office (NKFIH, Hungary)

M.E.S. acknowledge support in part from UK Science and Technology Facilities Council (STFC) grants ST/V000691/1 and ST/X001253/1.

This work was supported by an LSST Discovery Alliance LINCC Frameworks Incubator grant [2023-SFF-LFI-01-Schwamb]. Support was provided by Schmidt Sciences.

This work was supported by an LSST Discovery Alliance LINCC Frameworks Incubator grants [2025-SFF-LFI-01-Holman/2025-SFF-LFI-11-Schwamb]. Support was provided by Schmidt Sciences.

M.T.B. appreciate support by the Rutherford Discovery Fellowships from New Zealand Government funding, administered by the Royal Society Te Apārangi.

B.Carry is supported by INSU PNP.

T.D. acknowledges support from the McDonnell Center for the Space Sciences at Washington University in St. Louis.

R.C.D. is funded by grant #361233 awarded by the Research Council of Finland to M. Granvik.

The Science Fund of the Republic of Serbia through Project No. 7453 *Demystifying enigmatic visitors of the near-Earth region (ENIGMA)*

The views expressed in this article are those of the authors and do not reflect the official policy or position of the U.S. Naval Academy, Department of the Navy, the Department of Defense, or the U.S. Government.

This material is based in part on work done by M. Womack while serving at the National Science Foundation.

EW is supported by the National Science Foundation Graduate Research Fellowship Program under Grant No. 1000383199. Any opinions, findings, and conclusions or recommendations expressed in this material are those of the author(s) and do not necessarily reflect the views of the National Science Foundation.

FBR acknowledges CNPq grant 316604/2023-2.

R.M. acknowledges research funding from NASA grant 80NSSC21K0593.

CLP thanks the FAPERJ/PDR-10 E-26/200.107/2025 and FAPERJ 200.108/2025.

The authors acknowledge support from the DiRAC Institute in the Department of Astronomy at the University of Washington. The DiRAC Institute is supported through generous gifts from the Charles and Lisa Simonyi Fund for Arts and Sciences, Janet and Lloyd Frink, and the Washington Research Foundation.

The Catalina Sky Survey is funded by NASA's Planetary Defense Coordination Office, under grant 80NSSC24K1187.

CEH is supported by an LSST-DA Catalyst Fellowship, made possible by Grant 62192 from the John Templeton Foundation.

MJP acknowledges support from the NASA Minor Planet Center Award 80NSSC22M0024.

D.Z.S. is supported by an NSF Astronomy and Astrophysics Postdoctoral Fellowship under award AST-2303553. This research award is partially funded by a generous gift of Charles Simonyi to the NSF Division of Astronomical Sciences. The award is made in recognition of significant contributions to Rubin Observatory's Legacy Survey of Space and Time.

This material is based upon work supported by the National Science Foundation under grant No. AST-2406527.

J. M. acknowledges support from the Department for the Economy (DfE) Northern Ireland postgraduate studentship scheme and travel support from the STFC for UK participation in LSST through grant ST/S006206/1. J. M. thanks the LSST-DA Data Science Fellowship Program, which is funded by LSST-DA, the Brinson Foundation, the WoodNext Foundation, and the Research Corporation for Science Advancement Foundation; his participation in the program has benefited this work.

J.L. acknowledges support from the Agencia Estatal de Investigacion del Ministerio de Ciencia e Innovación (AEI-MCINN) under grant "Hydrated Minerals and Organic Compounds in Primitive Asteroids" with reference PID2020-120464GB-100.

FS acknowledges support from the NASA Minor Planet Center Award 80NSSC22M0024.

Work supported by Department of Energy contract DE-AC02-76SF00515.

SL is supported by the U.S. Department of Energy under grant number DE-1161130-116-SDDTA and under Contract No. DE-AC02-76SF00515 with the SLAC National Accelerator Laboratory.

The work of AAPM was supported by the U.S. Department of Energy under contract number DE-AC02-76SF00515. AAPM thanks the Department of Physics and the Laboratory of Particle Astrophysics and Cosmology of Harvard University, the Cosmology Group at Boston University, and the Department of Physics at Washington University in St. Louis for their hospitality during the preparation of this paper.

MJJ acknowledges support for the current research from the National Research Foundation (NRF) of Korea under the programs 2022R1A2C1003130 and RS-2023-00219959.

This work was supported in part by the LSST Discovery Alliance Enabling Science grants program, the B612 Foundation, the University of Washington's DiRAC In-

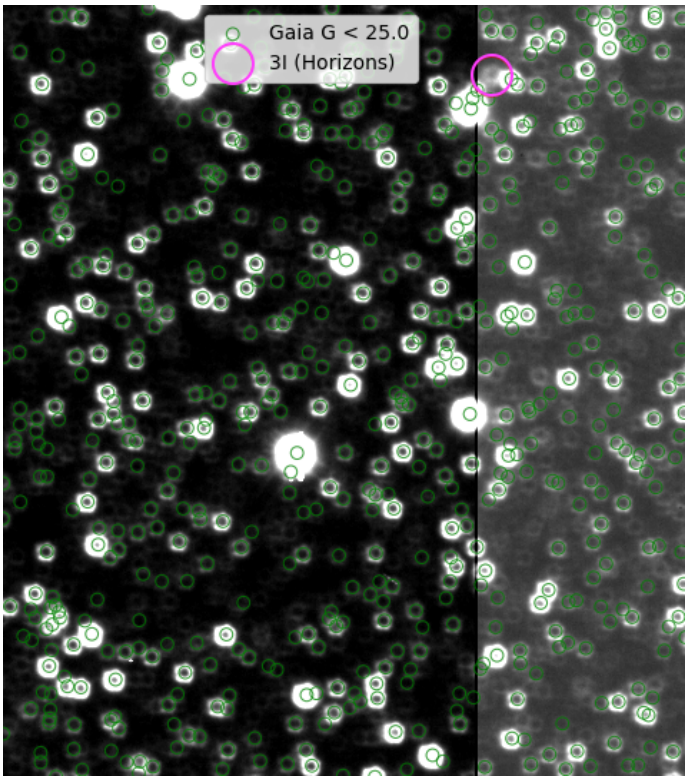


Figure A1. UT 2025 June 24, 30 s raw *i*-band exposure. The image was unintentionally out of focus during a science exposure, which is understandable given the current phase of commissioning of the AOS. The JPL Horizons calculated position of 3I/ATLAS is indicated by a magenta circle. Green circles indicate the Gaia DR3 stars in the FOV; there were no Gaia sources coinciding with the location of 3I/ATLAS. The FOV is 120″ high by 106.6″ wide.

stitute, the Planetary Society, Karman+, and Breakthrough Listen through generous support of the LSST Solar System Readiness Sprints. Breakthrough Listen is managed by the Breakthrough Initiatives, sponsored by the Breakthrough Prize Foundation (http://www.breakthroughinitiatives.org).

Facilities: Rubin:Simonyi (LSSTCam)

Software: astropy (Robitaille et al. 2013), `astrometry.net` (Lang et al. 2010), `ChatGPT` (coding) (OpenAI 2023), `Grammarly`, `JPL Horizons` (Giorgini et al. 1996), `Matplotlib` (Hunter 2007), `NumPy` (Harris et al. 2020), `pandas` (Reback et al. 2022), `PyTorch` (Paszke et al. 2019), `rubin_scheduler`, (Naghib et al. 2019; Yoachim et al. 2025a) `rubin_sim`, (Jones et al. 2014; Yoachim et al. 2025b) `SAOImageDS9` (Joye 2006), `SCARLETT` (Melchior et al. 2018), `SciPy` (Virtanen et al. 2020) `Siril`[10], `SkyBot` (Berthier et al. 2006), `sbpy` (Mommert et al. 2019), `Sorcha` (Merritt et al. 2025; Holman et al. 2025), `numba` (Lam et al. 2015), `uncertainties` (version 3.0.2), a `python` package for calculations with uncertainties by E. O. Lebigot[11], `find_orb` (Gray 2022), `astroquery` (Ginsburg et al. 2019), `GRSS`(Makadia et al. 2025)

APPENDIX

A. ADDITIONAL IMAGES

Figure A1 shows an out-of-focus science image from UT 2025 June 24.

[10] https://siril.org
[11] http://pythonhosted.org/uncertainties/

B. ESTIMATED COLOR CALCULATIONS

Since the vast majority of the observations reported in this work were not obtained in the expected two filter pairs as the observatory was still in commissioning, there are very few observations taken in different filters within a short period of time (cf Table 1). This makes the determination of the colors from Rubin data alone insufficiently robust, given the evolution of activity and colors with changing distance and corresponding activity. This is coupled with additional uncertainty on potential rotational variation and potential contamination by background sources (as discussed in Section 4.7. Recalling that Seligman et al. (2025) and Opitom et al. (2025) independently reported spectral gradients of $S' \sim 18\%/100$ nm for 3I/ATLAS (Section 1.2), we use this spectral gradient to compute equivalent colors for the object in the LSST *ugrizy* filter set (which differs from the SDSS filter system). Using the `spectroscopy` module[12] in `sbpy` and effective central wavelengths for LSST filters from the LSST website[13], we compute colors for 3I/ATLAS for each filter pair for a spectral gradient of $S' = 18\%/100$ nm (normalized at the central wavelength of the g'-band filter, or 480.69 nm) and show these in Table A1. For reference, in the same table, we also show solar colors in LSST filters that were computed from a Kurucz (1993) model spectrum of the Sun for use in the computation of the object's colors from its spectral gradient.

Table A1. Solar and Expected 3I/ATLAS colors in LSST filters

Color	Solar	3I/ATLAS[a]
$(u-g)_{\rm LSST}$	1.154	1.384
$(g-r)_{\rm LSST}$	0.436	0.677
$(r-i)_{\rm LSST}$	0.112	0.299
$(i-z)_{\rm LSST}$	0.011	0.147
$(z-y)_{\rm LSST}$	0.009	0.125

[a] Expected colors in LSST filters for 3I/ATLAS assuming a spectral gradient of $S' = 18\%$

C. ORBIT PARAMETERS

MPC Solution 20250715 orbit parameters and covariances for 3I/ATLAS derived from Minor Planet Center astrometry submitted by July 15, 2025 19:00 UTC are shown in Table B1. One-arcsecond weights for astrometric observations have been applied which lead to (normalized) root mean square (RMS) of the residuals of 0.3876. Here, 9 observations out of 1090 were rejected.

The results of a more aggressive outlier rejection scheme (579 rejections) are presented in Table B2. Here, Rubin astrometry was weighted at 250mas. In this case, post-fit residual RMS decrease to 0.27225, and the remaining bias of Rubin data becomes 9.0 mas RAcos(Dec) and -66.1 mas Dec.

Table B1. Orbital Parameters for 3I/ATLAS at epoch MJD 60800.0 TT, MPC Solution 20250715

	q [au]	e	i [deg]	Ω [deg]	ω [deg]	T_p [MJD, TT]
	1.3568940	6.1427557	175.112869	322.1560560	128.000675	60977.4773807
	±0.0012	±0.0086	±0.0006	±0.0116	±0.0117	±0.0176
	Covariance Matix					
	q	e	i	Ω	ω	T_p
q	1.2660×10^{-6}	9.6369×10^{-6}	5.1441×10^{-7}	1.1613×10^{-5}	-1.1753×10^{-5}	-1.9398×10^{-5}
e	9.6369×10^{-6}	7.3565×10^{-5}	3.9452×10^{-6}	8.8866×10^{-5}	-8.9124×10^{-5}	-1.4923×10^{-4}
i	5.1441×10^{-7}	3.9452×10^{-6}	3.6236×10^{-7}	6.8283×10^{-6}	-2.6919×10^{-6}	-8.1043×10^{-6}
Ω	1.1613×10^{-5}	8.8866×10^{-5}	6.8283×10^{-6}	1.3560×10^{-4}	-7.9137×10^{-5}	-1.8145×10^{-4}
ω	-1.1753×10^{-4}	-8.9124×10^{-5}	-2.6919×10^{-6}	-7.9137×10^{-5}	1.3745×10^{-4}	1.7758×10^{-4}
T_p	-1.9398×10^{-5}	-1.4923×10^{-4}	-8.1044×10^{-6}	-1.8145×10^{-4}	1.7758×10^{-4}	3.0918×10^{-4}

[12] https://sbpy.readthedocs.io/en/stable/sbpy/spectroscopy/index.html
[13] https://rubinobservatory.org/for-scientists/rubin-101/instruments

Table B2. Orbital Parameters for 3I/ATLAS at epoch MJD 60860.0 [TDB], Rubin Solution 20250715

	q [au]	e	i [deg]	Ω [deg]	ω [deg]	T_p [MJD, TDB]
	1.3578723	6.1505022	175.1132481	322.1641750	127.9905280	60977.4601065
	± 0.0012	± 0.0095	± 0.0006	± 0.01265	± 0.01315	± 0.0199
Covariance Matix						
	q	e	i	Ω	ω	T_p
q	1.5247×10^{-6}	1.1719×10^{-5}	1.0400×10^{-8}	2.3938×10^{-7}	-2.5245×10^{-7}	-2.4199×10^{-5}
e	1.1719×10^{-5}	9.0322×10^{-5}	8.0530×10^{-8}	1.8493×10^{-6}	-1.9338×10^{-6}	-1.8784×10^{-4}
i	1.0400×10^{-8}	8.0530×10^{-8}	1.3070×10^{-10}	2.4502×10^{-9}	-9.1417×10^{-10}	-1.6957×10^{-7}
Ω	2.3938×10^{-7}	1.8493×10^{-6}	2.4502×10^{-9}	4.8774×10^{-8}	-2.8591×10^{-8}	-3.8702×10^{-6}
ω	-2.5245×10^{-7}	-1.9338×10^{-6}	-9.1417×10^{-10}	-2.8591×10^{-8}	5.2731×10^{-8}	3.9572×10^{-6}
T_p	-2.4199×10^{-5}	-1.8784×10^{-4}	-1.6957×10^{-7}	-3.8702×10^{-6}	3.9572×10^{-6}	3.9820×10^{-4}

REFERENCES

A'Hearn, M. F., Schleicher, D. G., Millis, R. L., Feldman, P. D., & Thompson, D. T. 1984, AJ, 89, 579, doi: 10.1086/113552

Alarcon, M. R., Serra-Ricart, M., Licandro, J., et al. 2025, Deep g'-band Imaging of Interstellar Comet 3I/ATLAS from the Two-meter Twin Telescope (TTT), The Astronomer's Telegram, No. 17264. https://www.astronomerstelegram.org/?read=17264

Alard, C., & Lupton, R. H. 1998, ApJ, 503, 325, doi: 10.1086/305984

Alvarez-Candal, A., & Licandro, J. 2006, A&A, 458, 1007, doi: 10.1051/0004-6361:20064971

Alvarez-Candal, A., Rizos, J. L., Lara, L. M., et al. 2025, arXiv e-prints, arXiv:2507.07312, doi: 10.48550/arXiv.2507.07312

Bannister, M. T., Schwamb, M. E., Fraser, W. C., et al. 2017, ApJ, 851, L38, doi: 10.3847/2041-8213/aaa07c

Belton, M. J. S., Hainaut, O. R., Meech, K. J., et al. 2018, ApJL, 856, L21, doi: 10.3847/2041-8213/aab370

Bernardinelli, P. H., Bernstein, G. M., Jindal, N., et al. 2023, ApJS, 269, 18, doi: 10.3847/1538-4365/acf6bf

Berthier, J., Vachier, F., Thuillot, W., et al. 2006, in Astronomical Data Analysis Software and Systems XV ASP Conference Series, Vol. 351 (Orem, UT: Astronomical Society of the Pacific), 367

Bertin, E., & Arnouts, S. 1996, Astronomy and Astrophysics Supplement Series, 117, 393, doi: 10.1051/aas:1996164

Bianco, F. B., Jones, L., Ivezić, v., Ritz, S., & Rubin Project Science Team. 2022, Updated estimates of the Rubin system throughput and expected LSST image depth, Rubin Observatory Project Document PSTN-054. https://pstn-054.lsst.io

Bodewits, D., Noonan, J. W., Feldman, P. D., et al. 2020, Nature Astronomy, 4, 867, doi: 10.1038/s41550-020-1095-2

Bolin, B. T., Belyakov, M., Gray, C. L., et al. 2025, The Astronomer's Telegram, 17284, 1

Bolin, B. T., Weaver, H. A., Fernandez, Y. R., et al. 2018, ApJL, 852, L2, doi: 10.3847/2041-8213/aaa0c9

Bolin, B. T., Lisse, C. M., Kasliwal, M. M., et al. 2020, AJ, 160, 26, doi: 10.3847/1538-3881/ab9305

Bolin, B. T., Belyakov, M., Fremling, C., et al. 2025, Interstellar comet 3I/ATLAS: discovery and physical description. https://arxiv.org/abs/2507.05252

Borisov, G., Durig, D. T., Sato, H., & et al. 2019, Central Bureau Electronic Telegrams, 1

Bosch, J., Armstrong, R., Bickerton, S., et al. 2018, PASJ, 70, S5, doi: 10.1093/pasj/psx080

Bottke, W. F., Vokrouhlický, D., Marshall, R., et al. 2023, PSJ, 4, 168, doi: 10.3847/PSJ/ace7cd

Buie, M. W., Zangari, A. M., Marchi, S., Levison, H. F., & Mottola, S. 2018, AJ, 155, 245, doi: 10.3847/1538-3881/aabd81

Champagne, C., McClure, L., Emery, J., et al. 2025, The Astronomer's Telegram, 17283, 1

Chandler, C. O., Kueny, J. K., Trujillo, C. A., Trilling, D. E., & Oldroyd, W. J. 2020, The Astrophysical Journal Letters, 892, L38, doi: 10/gg36xz

Chandler, C. O., Trujillo, C. A., Oldroyd, W. J., et al. 2024, The Astronomical Journal, 167, 156, doi: 10.3847/1538-3881/ad1de2

Claver, C., Bauer, A., Bechtol, K., et al. 2025, Construction Completeness and Operations Readiness Criteria, Commissioning Technical Note SITCOMTN-005, NSF-DOE Vera C. Rubin Observatory. https://sitcomtn-005.lsst.io/

Cook, N. V., Ragozzine, D., Granvik, M., & Stephens, D. C. 2016, ApJ, 825, 51, doi: 10.3847/0004-637X/825/1/51

Cordiner, M. A., Milam, S. N., Biver, N., et al. 2020, Nature Astronomy, 4, 861, doi: 10.1038/s41550-020-1087-2

Cremonese, G., Fulle, M., Cambianica, P., et al. 2020, ApJL, 893, L12, doi: 10.3847/2041-8213/ab8455

de León, J., Licandro, J., Serra-Ricart, M., et al. 2019, Research Notes of the American Astronomical Society, 3, 131, doi: 10.3847/2515-5172/ab449c

de León, J., Licandro, J., de la Fuente Marcos, C., et al. 2020, MNRAS, 495, 2053, doi: 10.1093/mnras/staa1190

Deam, S. E., Bannister, M. T., Opitom, C., et al. 2025, arXiv e-prints, arXiv:2507.05051, doi: 10.48550/arXiv.2507.05051

Denneau, L., Siverd, R., Tonry, J., et al. 2025, MPEC

Dorsey, R. C., Hopkins, M. J., Bannister, M. T., et al. 2025, arXiv e-prints, arXiv:2502.16741, doi: 10.48550/arXiv.2502.16741

Drahus, M., Guzik, P., Waniak, W., et al. 2017, arXiv e-prints, arXiv:1712.00437, doi: 10.48550/arXiv.1712.00437

Eggl, S., Farnocchia, D., Chamberlin, A. B., & Chesley, S. R. 2020, Icarus, 339, 113596

Engelhardt, T., Jedicke, R., Vereš, P., et al. 2017, AJ, 153, 133, doi: 10.3847/1538-3881/aa5c8a

Farnham, T. L., Kelley, M. S. P., & Bauer, J. M. 2021, PSJ, 2, 236, doi: 10.3847/PSJ/ac323d

Farnocchia, D., Chesley, S. R., & Chamberlin, A. B. 2016, in AAS/Division for Planetary Sciences Meeting Abstracts, Vol. 48, AAS/Division for Planetary Sciences Meeting Abstracts #48, 305.03

Finson, M. J., & Probstein, R. F. 1968a, ApJ, 154, 327, doi: 10.1086/149761

Finson, M. L., & Probstein, R. F. 1968b, ApJ, 154, 353, doi: 10.1086/149762

Fitzsimmons, A., Meech, K., Matrà, L., & Pfalzner, S. 2023, arXiv e-prints, arXiv:2303.17980, doi: 10.48550/arXiv.2303.17980

Fitzsimmons, A., Hainaut, O., Meech, K. J., et al. 2019, The Astrophysical Journal Letters, 885, L9, doi: 10.3847/2041-8213/ab49fc

Flaugher, B., Diehl, H. T., Honscheid, K., et al. 2015, The Astronomical Journal, 150, 150, doi: 10.1088/0004-6256/150/5/150

Fraser, W. C., Pravec, P., Fitzsimmons, A., et al. 2018, Nature Astronomy, 2, 383, doi: 10.1038/s41550-018-0398-z

Gaia Collaboration, Vallenari, A., Brown, A. G. A., et al. 2023, A&A, 674, A1, doi: 10.1051/0004-6361/202243940

Ginsburg, A., Sipőcz, B. M., Brasseur, C. E., et al. 2019, AJ, 157, 98, doi: 10.3847/1538-3881/aafc33

Giorgini, J. D., Yeomans, D. K., Chamberlin, A. B., et al. 1996, American Astronomical Society, 28, 25.04

Graham, M. 2022, The Rubin Data Products, Abridged (2022), Zenodo, Version 2, doi: 10.5281/zenodo.7011229

Gray, B. 2022, Find_Orb: Orbit determination from observations, Astrophysics Source Code Library, record ascl:2202.016

Guzik, P., Drahus, M., Rusek, K., et al. 2020, Nature Astronomy, 4, 53, doi: 10.1038/s41550-019-0931-8

Hardorp, J. 1980, A&A, 91, 221

Harris, C. R., Millman, K. J., van der Walt, S. J., et al. 2020, Nature, 585, 357, doi: 10.1038/s41586-020-2649-2

Holman, M. J., Bernardinelli, P. H., Schwamb, M. E., et al. 2025, arXiv e-prints, arXiv:2506.02140, doi: 10.48550/arXiv.2506.02140

Hopkins, M. J., Bannister, M. T., & Lintott, C. 2025, AJ, 169, 78, doi: 10.3847/1538-3881/ad9eb3

Hopkins, M. J., Dorsey, R. C., Forbes, J. C., et al. 2025, From a Different Star: 3I/ATLAS in the context of the Ōtautahi-Oxford interstellar object population model. https://arxiv.org/abs/2507.05318

Hsieh, H. H., Ishiguro, M., Lacerda, P., & Jewitt, D. 2011, AJ, 142, 29, doi: 10.1088/0004-6256/142/1/29

Hsieh, H. H., & Jewitt, D. 2005, ApJ, 624, 1093, doi: 10.1086/429250

Hsieh, H. H., Denneau, L., Wainscoat, R. J., et al. 2015, Icarus, 248, 289, doi: 10.1016/j.icarus.2014.10.031

Hsieh, H. H., Noonan, J. W., Kelley, M. S. P., et al. 2025, PSJ, 6, 3, doi: 10.3847/PSJ/ad9199

Hui, M.-T., Ye, Q.-Z., Föhring, D., Hung, D., & Tholen, D. J. 2020, AJ, 160, 92, doi: 10.3847/1538-3881/ab9df8

Hunter, J. D. 2007, Computing in Science & Engineering, 9, 90, doi: 10.1109/MCSE.2007.55

Ivezić, Ž., Kahn, S. M., Tyson, J. A., et al. 2019, ApJ, 873, 111, doi: 10.3847/1538-4357/ab042c

Jewitt, D., Hui, M.-T., Kim, Y., et al. 2020, ApJL, 888, L23, doi: 10.3847/2041-8213/ab621b

Jewitt, D., & Luu, J. 2019, ApJL, 886, L29, doi: 10.3847/2041-8213/ab530b

—. 2025, Interstellar Interloper C/2025 N1 is Active, The Astronomer's Telegram, No. 17263. https://www.astronomerstelegram.org/?read=17263

Jewitt, D., Luu, J., Rajagopal, J., et al. 2017, ApJL, 850, L36, doi: 10.3847/2041-8213/aa9b2f

Jewitt, D., & Seligman, D. Z. 2023, ARA&A, 61, 197, doi: 10.1146/annurev-astro-071221-054221

Jones, L., Bianco, F. B., Yoachim, P., & Neilsen, E. 2025, https://survey-strategy.lsst.io, v0.1.0, Zenodo, doi: 10.5281/zenodo.15128504

Jones, R. L., Yoachim, P., Chandrasekharan, S., et al. 2014, in Society of Photo-Optical Instrumentation Engineers (SPIE) Conference Series, Vol. 9149, Observatory Operations: Strategies, Processes, and Systems V, ed. A. B. Peck, C. R. Benn, & R. L. Seaman, 0, doi: 10.1117/12.2056835

Jordi, K., Grebel, E. K., & Ammon, K. 2006, A&A, 460, 339, doi: 10.1051/0004-6361:20066082

Joye, W. A. 2006, in Astronomical Data Analysis Software and Systems XV ASP Conference Series, Vol. 351, 574–

Jurić, M., Kantor, J., Lim, K. T., et al. 2017, in Astronomical Society of the Pacific Conference Series, Vol. 512, Astronomical Data Analysis Software and Systems XXV, ed. N. P. F. Lorente, K. Shortridge, & R. Wayth, 279, doi: 10.48550/arXiv.1512.07914

Jurić, M., Axelrod, T., Becker, A. C., et al. 2023, Data Products Definition Document (LSE-163), LSST Project Document LSE-163, v3.9. https://ls.st/LSE-163

Kakharov, S., & Loeb, A. 2025, Galactic Trajectories of Interstellar Objects 1I/'Oumuamua, 2I/Borisov, and 3I/Atlas. https://arxiv.org/abs/2408.02739

Kim, Y., Jewitt, D., Mutchler, M., et al. 2020, ApJL, 895, L34, doi: 10.3847/2041-8213/ab9228

Knight, M. M., Kokotanekova, R., & Samarasinha, N. H. 2024, in Comets III, ed. K. J. Meech, M. R. Combi, D. Bockelée-Morvan, S. N. Raymodn, & M. E. Zolensky (University of Arizona Press), 361–404

Knight, M. M., Protopapa, S., Kelley, M. S. P., et al. 2017, ApJL, 851, L31, doi: 10.3847/2041-8213/aa9d81

Kokotanekova, R., Snodgrass, C., Lacerda, P., et al. 2017, MNRAS, 471, 2974, doi: 10.1093/mnras/stx1716

Kurucz, R. L. 1993, VizieR Online Data Catalog: Model Atmospheres (Kurucz, 1979), VI/39, VizieR Online Data Catalog. https://ui.adsabs.harvard.edu/abs/1993yCat.6039....0K

Lam, S. K., Pitrou, A., & Seibert, S. 2015, in Proceedings of the Second Workshop on the LLVM Compiler Infrastructure in HPC, 1–6

Lang, D., Hogg, D. W., Mierle, K., Blanton, M., & Roweis, S. 2010, Astronomical Journal, 139, 1782, doi: 10.1088/0004-6256/139/5/1782

Lim, K.-T. 2025, The Consolidated Database of Image Metadata, Data Management Technical Note DMTN-227, NSF-DOE Vera C. Rubin Observatory. https://dmtn-227.lsst.io/

Loeb, A. 2025, Comment on "Discovery and Preliminary Characterization of a Third Interstellar Object: 3I/ATLAS" [arXiv:2507.02757]. https://arxiv.org/abs/2507.05881

Luu, J. X., & Jewitt, D. C. 1992, Icarus, 97, 276, doi: 10.1016/0019-1035(92)90134-S

Makadia, R., Farnocchia, D., Chesley, S. R., & Eggl, S. 2025, The Planetary Science Journal, 6, 85

Marcus, J. N. 2007, International Comet Quarterly, 29, 39

Marčeta, D., & Seligman, D. Z. 2023, PSJ, 4, 230, doi: 10.3847/PSJ/ad08c1

Mashchenko, S. 2019, MNRAS, 489, 3003, doi: 10.1093/mnras/stz2380

McKay, A. J., Cochran, A. L., Dello Russo, N., & DiSanti, M. A. 2020, ApJL, 889, L10, doi: 10.3847/2041-8213/ab64ed

McNeill, A., Trilling, D. E., & Mommert, M. 2018, ApJL, 857, L1, doi: 10.3847/2041-8213/aab9ab

Meech, K. J., Weryk, R., Micheli, M., et al. 2017, Nature, 552, 378, doi: 10.1038/nature25020

Melchior, P., Moolekamp, F., Jerdee, M., et al. 2018, Astronomy and Computing, 24, 129, doi: 10.1016/j.ascom.2018.07.001

Merritt, S. R., Fedorets, G., Schwamb, M. E., et al. 2025, arXiv e-prints, arXiv:2506.02804, doi: 10.48550/arXiv.2506.02804

Micheli, M., Farnocchia, D., Meech, K. J., et al. 2018, Nature, 559, 223, doi: 10.1038/s41586-018-0254-4

Mommert, M., Kelley, M., de Val-Borro, M., et al. 2019, The Journal of Open Source Software, 4, 1426, doi: 10.21105/joss.01426

Moro-Martín, A. 2022, arXiv e-prints, arXiv:2205.04277, doi: 10.48550/arXiv.2205.04277

Naghib, E., Yoachim, P., Vanderbei, R. J., Connolly, A. J., & Jones, R. L. 2019, AJ, 157, 151, doi: 10.3847/1538-3881/aafece

Ochsenbein, F., Bauer, P., & Marcout, J. 2000, A&AS, 143, 23, doi: 10.1051/aas:2000169

OpenAI. 2023, ChatGPT (Mar 14, 2023 Version)

Opitom, C., Snodgrass, C., Jehin, E., et al. 2025, arXiv e-prints, arXiv:2507.05226, doi: 10.48550/arXiv.2507.05226

'Oumuamua ISSI Team, Bannister, M. T., Bhandare, A., et al. 2019, Nature Astronomy, 3, 594, doi: 10.1038/s41550-019-0816-x

Paszke, A., Gross, S., Massa, F., et al. 2019, in Advances in Neural Information Processing Systems, Vol. 32 (Curran Associates, Inc.)

Petit, J.-M., Gladman, B., Kavelaars, J. J., et al. 2023, ApJL, 947, L4, doi: 10.3847/2041-8213/acc525

Prodan, G. P., Popescu, M., Licandro, J., et al. 2024, MNRAS, 529, 3521, doi: 10.1093/mnras/stae539

Reback, J., jbrockmendel, McKinney, W., et al. 2022, Pandas-Dev/Pandas: Pandas 1.4.2, Zenodo, doi: 10.5281/zenodo.6408044

Robitaille, T. P., Tollerud, E. J., Greenfield, P., et al. 2013, Astronomy & Astrophysics, 558, A33, doi: 10/gfvntd

Rodionov, A. V., Jorda, L., Jones, G. H., et al. 1998, Icarus, 136, 232, doi: 10.1006/icar.1998.6010

Roodman, A., Rasmussen, A., Bradshaw, A., et al. 2024, in Society of Photo-Optical Instrumentation Engineers (SPIE) Conference Series, Vol. 13096, Ground-based and Airborne Instrumentation for Astronomy X, ed. J. J. Bryant, K. Motohara, & J. R. D. Vernet, 130961S, doi: 10.1117/12.3019698

Rubin Observatory Science Pipelines Developers. 2025, The LSST Science Pipelines Software: Optical Survey Pipeline Reduction and Analysis Environment, Project Science Technical Note PSTN-019, NSF-DOE Vera C. Rubin Observatory, doi: 10.71929/rubin/2570545

S. Deen, A. Hale, H. Sato, et al. 2025, Central Bureau Electronic Telegram No.5578: Comet C/2025 N1 (ATLAS) = 3I/ATLAS, Tech. Rep. CBET 5578, Central Bureau for Astronomical Telegrams, Hoffman Lab 209, Harvard University, Cambridge, MA 02138, U.S.A.

Schleicher, D. G., & Bair, A. N. 2011, AJ, 141, 177, doi: 10.1088/0004-6256/141/6/177

Schleicher, D. G., Millis, R. L., & Birch, P. V. 1998, Icarus, 132, 397, doi: 10.1006/icar.1997.5902

Sedaghat, N., & Mahabal, A. 2018, MNRAS, 476, 5365, doi: 10.1093/mnras/sty613

Seligman, D. Z., & Moro-Martín, A. 2022, Contemporary Physics, 63, 200, doi: 10.1080/00107514.2023.2203976

Seligman, D. Z., Micheli, M., Farnocchia, D., et al. 2025, Discovery and Preliminary Characterization of a Third Interstellar Object: 3I/ATLAS. https://arxiv.org/abs/2507.02757

Shi, X., Hu, X., Mottola, S., et al. 2018, Nature Astronomy, 2, 562, doi: 10.1038/s41550-018-0481-5

SLAC National Accelerator Laboratory, & NSF-DOE Vera C. Rubin Observatory. 2024, The LSST Commissioning Camera (LSSTComCam), SLAC National Accelerator Laboratory (SLAC), Menlo Park, CA (United States), doi: 10.71929/rubin/2561361

—. 2025, The LSST Camera (LSSTCam), SLAC National Accelerator Laboratory (SLAC), Menlo Park, CA (United States), doi: 10.71929/rubin/2571927

Stalder, B., Munoz, F., Aguilar, C., et al. 2024, in Society of Photo-Optical Instrumentation Engineers (SPIE) Conference Series, Vol. 13094, Ground-based and Airborne Telescopes X, ed. H. K. Marshall, J. Spyromilio, & T. Usuda, 1309409, doi: 10.1117/12.3019266

Taylor, A. G., & Seligman, D. Z. 2025, The Kinematic Age of 3I/ATLAS and its Implications for Early Planet Formation. https://arxiv.org/abs/2507.08111

Tonry, J. L., Denneau, L., Heinze, A. N., et al. 2018, PASP, 130, 064505, doi: 10.1088/1538-3873/aabadf

Trilling, D. E., Mommert, M., Hora, J. L., et al. 2018, AJ, 156, 261, doi: 10.3847/1538-3881/aae88f

Vera C. Rubin Observatory. 2025, The Vera C. Rubin Observatory Data Preview 1, doi: 10.71929/rubin/2570536

Vereš, P., Farnocchia, D., Chesley, S. R., & Chamberlin, A. B. 2017, Icarus, 296, 139

Virtanen, P., Gommers, R., Oliphant, T. E., et al. 2020, Nature Methods, 17, 261, doi: 10.1038/s41592-019-0686-2

Williams, G. V., Sato, H., Sarneczky, K., & et al. 2017, Central Bureau Electronic Telegrams, 1

Yang, B., Li, A., Cordiner, M. A., et al. 2021, Nature Astronomy, 5, 586–593, doi: 10.1038/s41550-021-01336-w

Ye, Q., Kelley, M. S. P., Bolin, B. T., et al. 2020, AJ, 159, 77, doi: 10.3847/1538-3881/ab659b

Ye, Q.-Z., Zhang, Q., Kelley, M. S. P., & Brown, P. G. 2017, ApJL, 851, L5, doi: 10.3847/2041-8213/aa9a34

Yoachim, P. 2025, lsst-sims/sims_featureScheduler_runs4.3: Initial Release, 1.0, Zenodo, doi: 10.5281/zenodo.14920193

Yoachim, P., Jones, L., Eric H. Neilsen, J., et al. 2025a, lsst/rubin_scheduler: v3.11.0, v3.11.0, Zenodo, doi: 10.5281/zenodo.15742506

—. 2025b, lsst/rubin_sim: v2.2.4, v2.2.4, Zenodo, doi: 10.5281/zenodo.15368965

Zackay, B., Ofek, E. O., & Gal-Yam, A. 2016, ApJ, 830, 27, doi: 10.3847/0004-637X/830/1/27

AOS Active Optics System
ATLAS Asteroid Terrestrial-impact Last Alert System
DDF Deep Drilling Field
GRSS Gauss-Radau Small-body Simulator
ISO Interstellar Object
KBO Kuiper Belt object
LSST Legacy Survey of Space and Time
MPC Minor Planet Center
MUSE Multi Unit Spectroscopic Explorer
PA position angle
PSF point spread function
RMS root-mean-square
SFD Size-Frequency Distribution
SNR signal to noise ratio
SSP Solar System Processing
SV Science Validation
ToO Target of Opportunity
VLT Very Large Telescope
WCS World Coordinate System
ZTF Zwicky Transient Facility